ACSNANO
www.acsnano.org
REVIEW

Contacts between Two- and Three-Dimensional Materials: Ohmic, Schottky, and *p*–*n* Heterojunctions

Yang Xu,*[,†,‡,⊥] Cheng Cheng,[†,⊥] Sichao Du,[†] Jianyi Yang,[†] Bin Yu,[†] Jack Luo,[†] Wenyan Yin,[†] Erping Li,[†] Shurong Dong,[†] Peide Ye,[§] and Xiangfeng Duan[‡]

[†]College of Information Science and Electronic Engineering, Zhejiang University, Hangzhou, Zhejiang 310027, China
[‡]Department of Chemistry and Biochemistry, University of California, Los Angeles, California 90095, United States
[§]School of Electrical and Computer Engineering, Purdue University, West Lafayette, Indiana 47906, United States

ABSTRACT: **After a decade of intensive research on two-dimensional (2D) materials inspired by the discovery of graphene, the field of 2D electronics has reached a stage with booming materials and device architectures. However, the efficient integration of 2D functional layers with three-dimensional (3D) systems remains a significant challenge, limiting device performance and circuit design. In this review, we investigate the experimental efforts in interfacing 2D layers with 3D materials and analyze the properties of the heterojunctions formed between them. The contact resistivity of metal on graphene and related 2D materials deserves special attention, while the Schottky junctions formed between metal/2D semiconductor or graphene/3D semiconductor call for careful reconsideration of the physical models describing the junction behavior. The combination of 2D and 3D semiconductors presents a form of *p*–*n* junctions that have just marked their debut. For each type of the heterojunctions, the potential applications are reviewed briefly.**

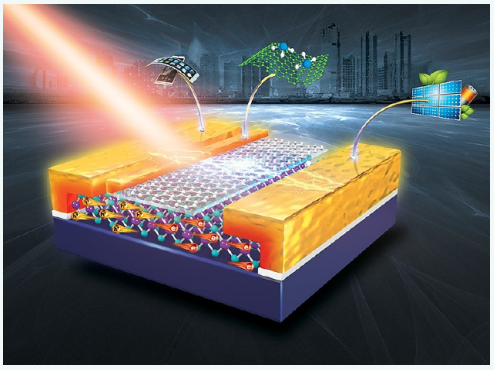

KEYWORDS: *2D materials, 3D materials, graphene, transition metal dichalcogenides, metals, transfer length method, Ohmic contact, Schottky, heterojunctions, sensors, detectors*

With the advent of various two-dimensional (2D) materials ranging from insulators, semiconductors, to metals, enormous efforts have been put into the investigation of their fundamental physical/chemical properties. They are expected to bring about revolutionary opportunities in nanoelectronics as the traditional silicon-based technology is reaching its physical limit.[1,2] Though relatively young, the field of 2D electronics has seen rapid development in a number of directions with high-impacting review articles already available,[3−6] especially on graphene[7−10] and 2D transition metal dichalcogenides (TMDs).[11,12] In parallel with the studies of intrinsic properties of monolayer 2D materials, the van der Waals (vdW) heterostructures have attracted special attention in the past 2−3 years.[13−16] The endless possibilities of stacking different 2D materials to create atomic scale heterostructures and superlattices can open up exciting opportunities for creating designed device architectures with tunable electronic properties beyond the reach of single material. In addition, with excellent electronic properties and exceptional mechanical robustness, 2D materials have also attracted considerable attention for a generation of highly flexible electronics with a combination of electronic performance and mechanical flexibility.[17−20]

While the "pure 2D" concept is revolutionary, interfacing 2D materials with the three-dimensional (3D) world[21] is never a subject that could be circumvented but somehow has not received enough attention. The most prominent issue might be the *contact resistance*.[22] Most of the investigations on intrinsic properties of 2D materials are carried out in the configuration of field-effect transistors (FETs). Without the careful selection of the contact metal along with optimized integration protocols, the channel properties of 2D materials could be masked easily by the contact resistance.[23,24] This artifact would be aggravated in the short-channel limit that is often necessary for high-performance devices,[25] which poses a critical challenge in device scaling. On the other hand, a considerable amount of work has been put into the Schottky junction devices formed between graphene (as transparent electrode) and conventional semiconductors or metal on 2D semiconductors, as will be

Received: March 16, 2016
Accepted: April 30, 2016
Published: April 30, 2016

DOI: 10.1021/acsnano.6b01842
ACS Nano 2016, 10, 4895−4919

discussed in the following sections. Despite the fact that these devices are different forms of Schottky junctions with charge carriers being transported from 2D (3D) to 3D (2D) material, the conventional 3D Schottky junction transport model has been commonly adapted to characterize the junction properties and functions as a fundamental guideline for device optimization.

In this review, we would like to point out that, in many cases, it might no longer be appropriate to analyze the 2D/3D interface based merely on conventional 3D models, as commonly practiced (note that 2D−2D contact is out of the scope of this review). There are four categories of 2D/3D contacts depending on the material type, upon which we divide our discussions into the following parts: (1) the metal contact on graphene, (2) the metal contact on 2D semiconductors (TMDs, black phosphorus (BP), silicene, *etc.*), (3) graphene on conventional semiconductors, and (4) 2D semiconductors on conventional semiconductors (Figure 1). In the first section, we

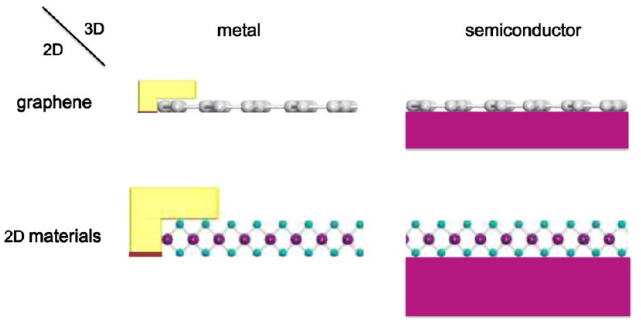

Figure 1. Outline of the review. The review concerns specifically the heterojunctions formed between a 2D and a 3D material. According to the material type (metal or semiconductor, either in 2D or 3D), the contacts are Ohmic, Schottky, or *p*−*n* junctions. The contact resistance problem is discussed thoroughly in the graphene/metal case, as well as in the 2D semiconductor/metal contacts.

focus on the contact resistance (R_C) problem on graphene. After a brief review of the conventional 3D transfer length method (TLM), we introduce the modified face-contact model proposed for the 3D metal/2D graphene system and move on to the edge-contact model studied more recently. Following the work on contacting graphene, we discuss the efforts made to contact 2D semiconductors in the second section. The third section covers the graphene/conventional semiconductor junctions. Until now, various semiconductors have been put in contact with graphene to form the Schottky diode, and nearly all of the studies rely on a classical 3D Schottky junction transport model to analyze their results. We introduce the most recent works concerning the modification of the Schottky diode model, taking into account the 2D nature of graphene and its tunable Fermi level under bias. In the last section, we summarize the limited number of articles available studying the *p*−*n* junction formed between a 2D semiconductor and a 3D semiconductor. This area of research is just emerging, but we expect to see a fast development here.

METAL ON GRAPHENE: OHMIC CONTACT

Contact Resistance. For the development of any electronic devices, making reliable electrical contact to the active layer is the first step. The precise characterization of the Ohmic contact or control over the Schottky contact is essential for probing the intrinsic transport properties of the channel material as well as improving the device performance. The electrical contact issue calls for close attention especially when ideal Ohmic contact is difficult to achieve, as is the case for emerging 2D electronic materials. Here, we start with the very basics of contact resistance characterization in conventional semiconductor devices and then review recent efforts in adapting these fundamental techniques into the nascent yet more complicated 2D cases.

Though graphene has been intensively investigated ever since its discovery in 2004,[26] it was not until around 2010 that the issue of contact resistance to graphene had received proper attention.[27] As a critical limiting factor of the on-current in graphene FETs, the contact resistance was characterized using the TLM commonly implemented in conventional semiconductor devices. Figure 2A illustrates the TLM configuration.

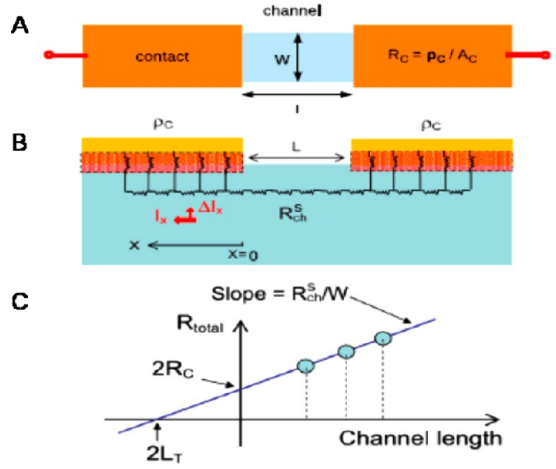

Figure 2. TLM for extracting the contact resistance R_C and the transfer length L_T in conventional semiconductor devices: (A) top view of the measurement configuration; (B) side view to show the resistive network for calculating L_T, and (C) $R_{total}(L)$ plot for extracting R_C and L_T.

The total resistance (R_{total}) of the contact(C)−channel(Ch)−contact(C) structure is measured with two probes, and $R_{total} = R_{Ch}{}^S(L/W) + 2R_C$, where $R_{Ch}{}^S$ is the sheet resistance, L is the length, and W is the width of the channel. By varying L, $R_{Ch}{}^S$ can be extracted from the slope of R_{total} as a function of L, as shown in Figure 2C. Meanwhile, the contact resistance R_C is characterized by the intercept of the fitted line on the y-axis. The specific contact resistivity ρ_C is defined conventionally as $R_C A_C$ in the unit of $\Omega\cdot cm^2$, where A_C is the contact area. Figure 2B illustrates the resistive network model used for extracting the transfer length L_T, another critical parameter in contacts. The current and the voltage along the x-direction can be solved using the equations

$$dI(x) = -\frac{V(x)}{\rho_C/(W\,dx)} \quad (1)$$

$$dV(x) = -I(x)R^S_{Ch}\left(\frac{dx}{W}\right) \quad (2)$$

and the results are

$$V(x) = V_0 e^{-x/L_T} \quad (3)$$

DOI: 10.1021/acsnano.6b01842
ACS Nano 2016, 10, 4895−4919

Table 1. Contact Resistivity ρ_C on Graphene Measured by TLM[a]

metal (thickness)	ρ_C ($\Omega\cdot cm^2$)	refs (year)	graphene type
Ni (25, 60 nm)	$\sim 10^{-5}$	27,28 (2010)	mechanically exfoliated
Cr, Ti/Au (10/20 nm)	10^{-4}–10^{-1}	28 (2010)	mechanically exfoliated
Ti/Au (10/50 nm)	$>10^{-5}$	29 (2011)	epitaxial on SiC
Ti, Ni, Cu, Pt, Pd/Au + "ash"	$<10^{-7}$	29 (2011)	epitaxial on SiC
Ti/Pt/Au	$\sim 10^{-8}$–10^{-7}	30 (2012)	epitaxial on SiC

[a]The Si industry requires $\sim 10^{-8}$ $\Omega\cdot cm^2$, and the short-channel graphene devices would require $\sim 10^{-10}$ $\Omega\cdot cm^2$.

$$I(x) = \frac{1}{R^S_{Ch}} \frac{W}{L_T} V_0 e^{-x/L_T} \quad (4)$$

where $L_T = (\rho_C/R^S_{Ch})^{1/2}$. Because of the resistance at the metal/channel interface and the channel sheet resistance, the current flows preferably close to the contact edge and drops to $1/e$ of the edge value at the length of L_T, a phenomenon known as "current crowding". The effective contact area is therefore defined as $L_T W$. Using L_T, the total resistance of the system can be expressed as $R_{total} = (R^S_{Ch}/W)(L + 2L_T)$. The intercept of the fitted $R_{total}(L)$ line with the x-axis gives L_T directly.

The specific contact resistivity of graphene measured using this TLM approach is summarized in Table 1. For contact lengths larger than L_T, current crowding is so significant that the contact resistivity is described more effectively as $R_C W$ in $\Omega\cdot\mu m$. The ρ_C is also affected by the metal type because the Fermi level shift in graphene on contacting metals has different work functions.[31] Various efforts have been made to improve contact to graphene devices, and low ρ_C values are reported.

Although the TLM is used regularly for characterizing the contact resistance R_C and the transfer length L_T at the face contact between graphene and metal, whether this 3D resistive network model is valid for a 2D–3D contact is questionable. Only through proper understanding of the electron transport mechanism and current flow at the contact can one improve ρ_C effectively, which has recently been systematically addressed by Xia *et al.*[32] In conventional TLM, there are two basic assumptions: (1) the metal/semiconductor contact is diffusive due to a very short electron mean free path in doped semiconductors, and (2) the sheet resistance of the semiconductor is identical in the transport channel or under the contact since the current flows in the bulk. However, neither of these assumptions holds true for graphene. As a result, the resistive network model is no longer appropriate for extracting the transfer length L_T, which characterizes the current crowding and is critical in contact design. Meanwhile, it is necessary to differentiate the sheet resistance in the channel and under the contact, as graphene is doped by the contact metal.

Figure 3 illustrates the model proposed for replacing the resistive network model shown in Figure 2B. It focuses on the transmission probability T at the two contact junctions: (1) the metal–graphene junction, T_{MG}, and (2) the p–n junction for graphene under the contact and in the channel, T_K. According to Landauer's approach, the conductance $G \propto TM$, where M is the number of conduction modes in graphene, is determined by the density of states (DOS) and its broadening due to inhomogeneities as well as coupling to the metal d states. When the electron is injected from graphene to metal, the coupling of graphene to metal induces the only scattering process in the ballistic limit, characterized by the effective coupling length λ_m. The transmission probability is $T_{MG} = \sqrt{\lambda/(\lambda_m + \lambda)}$, where λ is the electron mean free path in graphene. In the diffusive limit

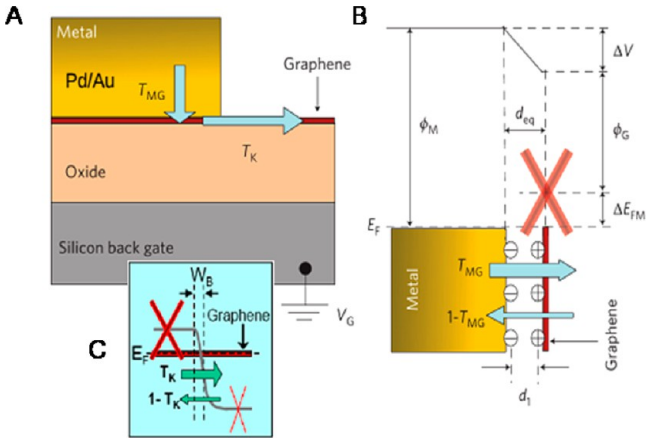

Figure 3. Transport at the metal/graphene contact proposed by Xia *et al.*[32] (A) Tansmission probabilities: T_{MG}, carrier injection from metal to graphene and T_K, from graphene under the contact to the channel. (B,C) Band diagram at the metal–graphene interface and the graphene p–n junction, respectively.

where $\lambda \ll \lambda_m$, $T_{MG} = \sqrt{\lambda/\lambda_m}$; in the ballistic limit ($\lambda \gg \lambda_m$), $T_{MG} \sim 1$. The effective transfer length L_T in this case is $\sqrt{\lambda\lambda_m}$. It is worth noting here that λ in graphene is significantly longer than that in conventional semiconductors, leading to a majorly ballistic transport at the metal/graphene interface. Therefore, the contact resistance shows a negative temperature dependence, in contrary to conventional semiconductors. Based on this model, to increase the contact conductance $G_C \propto TM$, either M could be increased by heavy doping of the graphene under the metal or T could be enhanced by increasing the mean free path λ in graphene and reducing the effective coupling length λ_m with the contact metal.

Current Flow between Contacts. In the contact resistance models discussed above, the metal electrodes act on the graphene layer in their immediate adjacency. On the other hand, as a layered anisotropic material (in-plane *vs* out-of-plane), graphene has unique distribution of current in multilayer channels compared with 3D isotropic materials, which in return influences the contact and gating behavior in devices. Sue and Appenzeller established the model of interlayer charge coupling and screening in multilayer graphene, which also provides insights to current flow in other 2D materials.[33] They presented the systematic experimental study on current distribution in multilayer graphene FETs by varying the channel layer number. As shown in Figure 4A, the on-state conductance of the channel G_{on} shows a decreasing trend with increasing layer number (channel thickness d), contrary to intuitions, while the off-state conductance G_{off} increases; the I_{on}/I_{off} shows a $1/d$ dependence.

The resistive network model illustrated in Figure 4B gives a satisfactory interpretation of the experimental data, composed

DOI: 10.1021/acsnano.6b01842
ACS Nano 2016, 10, 4895–4919

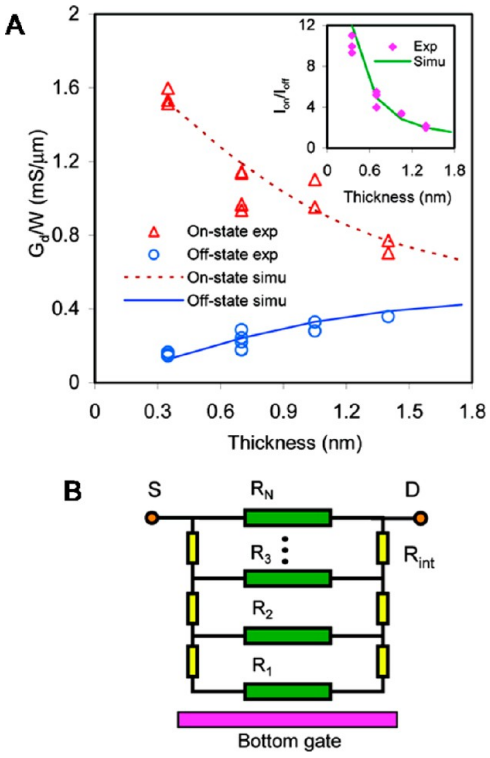

Figure 4. Resistive network model for current distribution in multilayer graphene FET. (A) Experimental data of the current on/off ratio (inset), the on- and off-channel conductance, and the fitted line using the model shown in (B); each layer has its resistance R_i, and the interlayer resistance is R_{int}.[33]

of intralayer resistance R_1 to R_N for N layers of graphene and interlayer resistance R_{int}. Each layer has a minimum conductance G_{min} regardless of the gating condition, and the ratio between R_{int} and the off-state single-layer resistance R_{off} is estimated to be $R_{int}/R_{off} \sim 0.02-0.2$. When the FET is gated, the total charge on the gate is Q_{gate}, and the vertical (z) Coulomb potential in the channel $\varphi(z) \propto (Q/z)\exp(-z/\lambda)$, where Q is the charge under Thomas–Fermi screening and λ is the screening length. Therefore, we have

$$Q_i \propto \frac{1}{t_{ox}+r_i}\exp\left(-\frac{t_{ox}+r_i}{\lambda}\right) \tag{5}$$

$$\sum_{i=1}^{N} Q_i = Q_{gate} \tag{6}$$

where Q_i is the charge in the ith layer, t_{ox} is the dielectric thickness, and r_i is the distance from the dielectric/channel interface to the ith layer. Assuming the conductance in each layer is proportional to the charge induced in it, we have

$$G_{on,i} = \frac{c^{i-1}}{\sum_{j=1}^{N} c^{j-1}} G_{gate} + G_{min} \tag{7}$$

where

$$c = \frac{Q_i}{Q_{i-1}} \approx \exp\left(-\frac{r_i - r_{i-1}}{\lambda}\right) \tag{8}$$

and G_{gate} corresponds to the conductance under total gate charge.

In this model, the two critical parameters are the ratio R_{int}/R_{off}, characterizing the interlayer coupling, and the screening length λ. The fitting results shown in Figure 4A uses $R_{int} = 0.05R_{off}$ and $\lambda = 0.6$ nm, suggesting a short depth of the current flow from the top contact into the bulk of the multilayer channel and rather limited gate control across the channel thickness since λ extends only two graphene layers.

Improving the Contact: Surface or Edge? Based on the models discussed above, it is clear that the interlayer tunneling of electrons limits the contact conductance in a metal/graphene system significantly, due to the lack of bonding sites at the surface of graphene. An alternative strategy is then to utilize the edge contact. Wang *et al.* reported the device topology in which the encapsulated 2D graphene channel makes pure one-dimensional (1D) edge contact to the 3D metal electrodes (Figure 5).[34] The device shows 25% less specific contact resistance (Cr/Pd/Au 1/15/60 nm, ~150 Ω·μm) compared with that reported in ref 32 and other intrinsic face contacts and demonstrates almost ideal transport over length scales longer than 15 μm at low temperatures. The much improved contact is attributed to the shorter bonding distance at the metal/

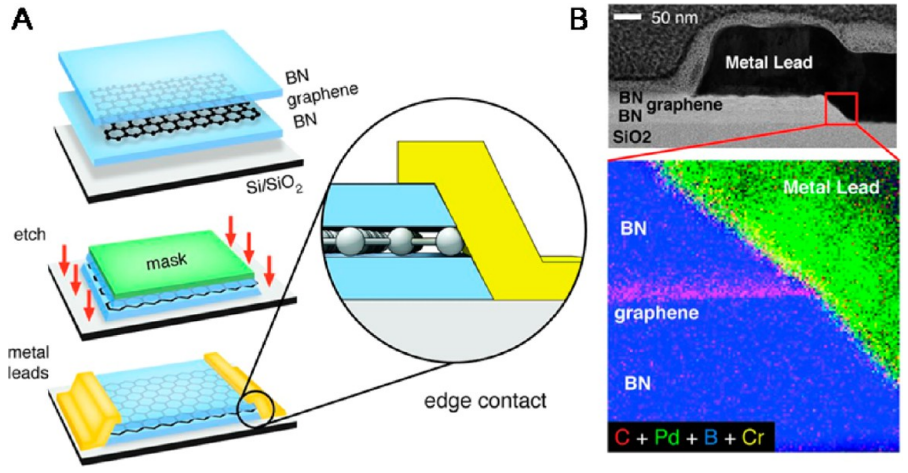

Figure 5. Edge contact to graphene. (A) Graphene monolayer is encapsulated between boron nitride to expose the edge, followed by regular deposition of Cr/Pd/Au (1/15/60 nm) to form the edge contact. (B) Scanning transmission electron microscopy image (top panel) and electron energy loss spectroscopy map (bottom panel) confirming the edge-contact formation.[34]

DOI: 10.1021/acsnano.6b01842
ACS Nano 2016, 10, 4895–4919

Table 2. Contact Resistivity on Graphene with Edge Contact

metal (thickness)	ρ_C ($\Omega\cdot\mu$m)	ref (year)	graphene type
Cr/Pd/Au (1/15/60 nm)	150, *25% reduction of ref 20	34 (2013)	mechanically exfoliated
Cu	~150, *32% reduction	35 (2013)	epitaxial on SiC
Pd	~457, *22% reduction	35 (2013)	epitaxial on SiC
Ni	89−11	36 (2014)	mechanically exfoliated
Pd/Au (20/30 nm)	2.2×10^{-9} $\Omega\cdot cm^2$	37 (2014)	CVD
Ti	7.7×10^{-8} $\Omega\cdot cm^2$	38 (2015)	CVD, multilayer

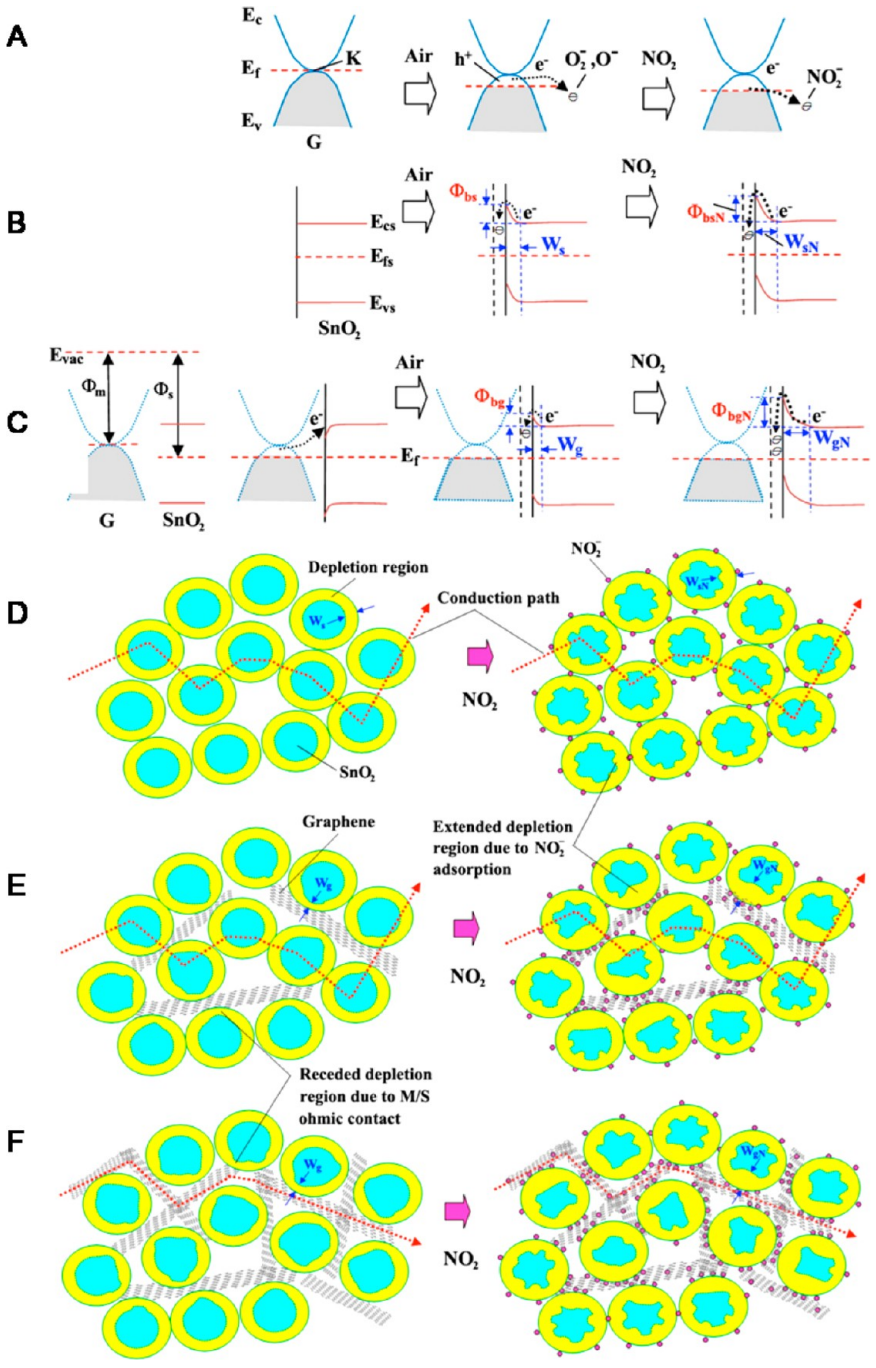

Figure 6. Energy band diagrams for sensing NO_2 gas with (A) graphene, (B) SnO_2 surface, and (C) graphene−SnO_2 interface. Schematic mechanisms of (D) SnO_2 NPs, (E) less graphene interacting with SnO_2 NPs, and (F) more graphene interacting with SnO_2 NPs.[55]

graphene edge, leading to larger electron orbital overlap, which is also consistent with Xia's strategy of reducing λ_m, the effective graphene−metal coupling length.[32]

Following this demonstration of effective 1D contact and previous analysis on "current crowding", much work has been done to improve the contact to graphene based on the increase

DOI: 10.1021/acsnano.6b01842
ACS Nano 2016, 10, 4895−4919

of the edge perimeter in the contact area, often followed by postmetal deposition annealing to aid the covalent bonding of carbon and metal atoms at the graphene crystal edges. The results are shown in Table 2.

Applications. *Photodetection.* As mentioned in the Contact Resistance section, the contact metal dopes the graphene and therefore shifts its Fermi level locally, due to the difference in the metal/graphene work function as well as the limited DOS near the graphene Dirac point. In a graphene FET, the Fermi level E_F in the graphene under the metal contact is determined by the charge transfer from the metal and not affected by the gate. The Fermi level in the channel aligns with this E_F; however, its doping level is controlled by the gate. An energy difference in the Dirac point is thus established between the graphene under the contact and in the channel, leading to band bending and therefore a built-in electric field at the contact/channel interface.

Utilizing this built-in field to separate the photogenerated carriers, Xia *et al.* demonstrated the pioneering work elucidating the influence of metal contacts on photocurrent generation in backgated graphene FETs.[39] Ghosh *et al.*'s work on reduced graphene oxide for position-dependent photodetection also supports this physical picture.[40] This device concept further led to the high-frequency study by the same group.[41] Urich *et al.* investigated the ultimate high-frequency response of the graphene photodetectors in the same layout, extracting the intrinsic response time *via* a nonlinear photocurrent autocorrelation signal and gave a bandwidth of ~262 GHz, corresponding to a photodetection response time of 2.1 ps, which is mainly limited by the lifetime of the photogenerated carriers.[42] To investigate directly the temporal response at the metal/graphene interface, Prechtel *et al.* introduced the pump–probe technique in a suspended chemical vapor deposition (CVD) graphene device and measured a photocurrent with a full width at half-maximum (fwhm) of ~4 ps originating from the built-in electric field.[43] Echtermeyer and co-workers further elucidated the photoelectric and photothermoelectric contributions to the photocurrent based on angular-dependent measurements using linearly polarized light, observing more prominent photoelectric effects at longer wavelengths,[44] which is also consistent with the report by Tielrooij *et al.*[45] The limiting factors of the photodetection responsivity (typically less than 1 mA/W) in the photocurrents generated at the two electrodes are of opposite sign, and the total current is nearly diminished. Mueller *et al.* circumvented this issue by using asymmetric metal contacts at the source and the drain.[46]

Gas Sensing. A number of graphene-based devices for detecting various gas species have been demonstrated,[47−49] as graphene possesses high surface-to-volume ratio in conjunction with high conductivity, leading to the sensitive molecule detection on its surface.[50] The electrons are accepted or donated from gas molecules to increase or decrease the channel conductance of the devices. Even though the graphene-based devices show high sensitivity, the difficulty of determining the type of the gas species and their concentration prevents the implementation of graphene as gas sensors.

Therefore, metal or metal oxide nanoparticles (NPs) have been introduced into the device structure recently.[51,52] The interaction between metal NPs and graphene shifts the Fermi level of graphene in order to achieve equilibrium with metal NPs. These NPs in the form of a thin film contacted with the graphene are expected to improve the selectivity of the gas sensors because different metals on graphene result in different electrical conductivity and surface functions. Ohmic characteristics have generally been observed.[50]

Chung *et al.* fabricated a flexible H_2 sensor using graphene with Pd NPs.[53] The optimized 3 nm thick Pd NP film shows a 33% gas response exposed to 1000 ppm of H_2, and the detection limit is 20 ppm of H_2 at room temperature. They suggested that the sensor response time could be improved by optimizing sample preparation, for instance, the control over the size/density of Pd NPs with patterned graphene in nanometer width. Park *et al.* used a periodic 200 nm wide graphene nanoribbon array with 1 μm pitch to protect the graphene from photoresist contamination on its surface by implementing a 10 nm thick Cr interlayer.[54] The fabricated Pd NP/graphene nanoribbon H_2 gas-sensing device exhibits 90% response within 60 s at 1000 ppm and 80% recovery within 90 s in ambient N_2. Detailed mechanisms were proposed by Tammanoon *et al.* on the basis of the formation of Ohmic M–S contacts and accessible interfaces of graphene–SnO_2 NPs.[55] The band diagram and physical models are as depicted in Figure 6. The synergistic metal NPs in contact with graphene modulates the overall electronic properties, leading to a significant enhancement of selectivity and sensitivity in gas-sensing characteristics. In addition to various metal NPs, graphene with different formats, for instance, pristine graphene, graphene oxide, and reduce graphene oxide (RGO) has also been investigated.[49,50,52] Chu *et al.* obtained high H_2 sensitivity with a resistance decrease of more than 80% in response to 1% H_2 at room temperature.[56] The sensor showed good selectivity toward H_2 over CH_4, NH_3, O_2, and N_2O. Vedala *et al.* found that the presence of holes in the basal plane of the RGO created edges with O_2 functionalities that significantly enhanced the response of Pt NP/holey RGO to H_2.[49]

An increase in device conductance for increasing H_2 concentrations was attributed to the interfacial interactions of H_2 with quinone groups located at the edges of the Pt NP/holey RGO system. In Lu *et al.*'s work on the detection of NO_2/NH_3 using RGO FETs, the authors pointed out that in addition to the charge transfer between the RGO and the adsorbed gas molecules, the variation in the Schottky barrier between the RGO and the contact metal, due to the gas absorption, could also contribute to the overall gas-sensing response.[57]

METAL CONTACT TO 2D SEMICONDUCTORS

Based on the studies done on graphene, the metal contact to other 2D materials, especially 2D semiconductors such as TMDs (MoS_2, $MoSe_2$, WS_2, *etc.*) and BP, has seen a surge of research activities in recent years. Unlike graphene, these 2D semiconductors have tunable band gaps covering both the narrow (~10^{-1} eV, BP) and wide (1–2 eV, TMD) regimes, providing great potential for various device applications. Metal forms Schottky contact to 2D semiconductors, which will be discussed in this section. MoS_2 represents one of the most frequently studied 2D semiconductors. Therefore, we will focus our systematic discussions on MoS_2 along with brief introduction on more recent works of BP/phosphorene.

As the electron mean free path is much shorter in TMDs, the TLM can be applied with a modified TLM model. Three factors should be considered when applying the TLM model. First, the contact resistance is a combination of the metal–semiconductor interface resistivity and the semiconductor sheet resistivity. However, the metal electrodes can easily dope and tune the atomic thin channels of 2D TMD semiconductors

DOI: 10.1021/acsnano.6b01842
ACS Nano 2016, 10, 4895–4919

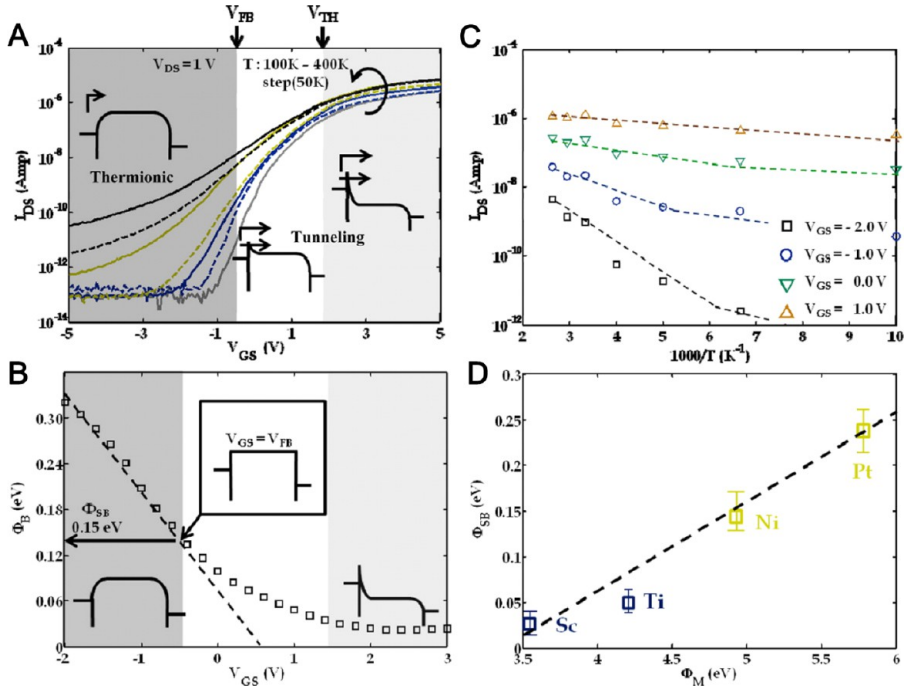

Figure 7. Extraction of the SBH at the Ni/MoS_2 junction. (A) Source−drain current as a function of the backgate voltage under fixed V_{DS}, at different temperatures. (B) Effective barrier height φ_B as a function of the backgate voltage. (C) Arrhenius-type plot of data in (A). (D) True SBH φ_{SB} extracted for different work function metals.[23]

underneath through the applied biases, thus making the contact resistivity complicated. For this reason, the resistivity of semiconducting TMDs under the metal contact ($\rho_{contact}$) and the resistivity of the semiconducting channel ($\rho_{channel}$) might be very different. Second, because of current crowding effects, the transfer length (L_T) and physical metal−semiconductor contact length (L_c) should be characterized case by case when applying effective contact length to the TLM model. Third, the TLM approach cannot accurately model metal contact to multi-2D layers if the edge contacts dominate the contact resistance. Most of metal/TMD 2D materials are Schottky contacts, which lead to the measured two-point resistance from TLM depending on the voltage bias and polarization.

Initial Contact with MoS_2. Das *et al.* performed the thorough experimental study of contacts to mechanically exfoliated few-layer MoS_2,[23] comparing the Schottky barrier height (SBH) and the FET performance using different contact metals: the low work function of Sc (φ_M = 3.5 eV, 30 nm Sc/20 nm Ni) and Ti (4.3 eV, 50 nm) and the high work function of Ni (5.0 eV, 50 nm) and Pt (5.9 eV, 50 nm). Figure 7 illustrates the details of extracting the SBH φ_{SB} at the Ni/MoS_2 interface from the FET characteristics. The temperature-dependent I_{DS} at each fixed gate voltage V_{GS} gives the Arrhenius plot (Figure 7B), from which the effective barrier height φ_B at certain V_{GS} is extracted using the high-temperature data. The linear regime of φ_B as a function of V_{GS} indicates that the thermionic emission model applies well to the current (Figure 7C). The true SBH φ_{SB} shows linear dependence on the metal work function φ_M, as shown in Figure 7D, with slope of 0.1, indicating strong Fermi level pinning at the metal/MoS_2 interface.

To quantify the metal/2D semiconductor contact resistance, the resistive network model is very much in parallel to the work done for graphene, although the graphene/metal contact is Ohmic while the 2D semiconductor/metal contact is Schottky and shows much higher contact resistivity ρ_C in the range of kΩ·μm to MΩ·μm. In the backgated FET configuration, Liu *et al.* used the conventional TLM to characterize the contact resistivity ρ_C and transfer length L_T of monolayer CVD MoS_2 contacted with Ti/Au.[58] The transfer length was calculated as $\sqrt{\rho_C/R_{sh}}$, where R_{sh} is the sheet resistance of monolayer MoS_2. At 0 V backgate, $L_T \sim 1.26$ μm, and at higher V_{bg}, $L_T \sim 0.63$ μm. The transistor performance is controlled by two Schottky barriers at the source and the drain, respectively, and the device is more accurately described as a Schottky barrier transistor, as illustrated in Figure 8. The Fermi level pinning between MoS_2

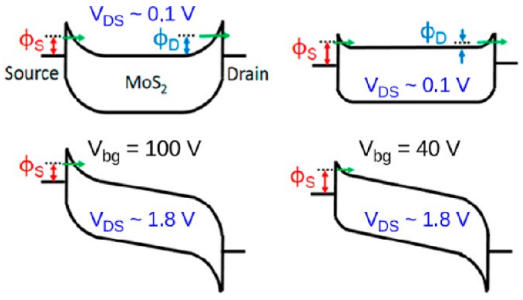

Figure 8. Band diagrams for a Ti/Au contacted MoS_2 FET with a backgate, showing the Schottky barriers at the source and the drain under different V_{bg} and V_{DS}.[58]

and the electrode is mainly caused by the gap states from the intralayer S−Mo bonding and the presence of a metal−MoS_2 alloy with a different work function.[59] It is very difficult to eliminate this effect because it requires an ideal Schottky contact between metal and a perfect 2D semiconductor crystal. Improving the signal crystal quality of the 2D semiconductor is an important but challenging choice to weaken the Fermi level pinning. Decoupling the metal from the semiconductor surface can also decrease the amount of Fermi level pinning. An

DOI: 10.1021/acsnano.6b01842
ACS Nano 2016, 10, 4895−4919

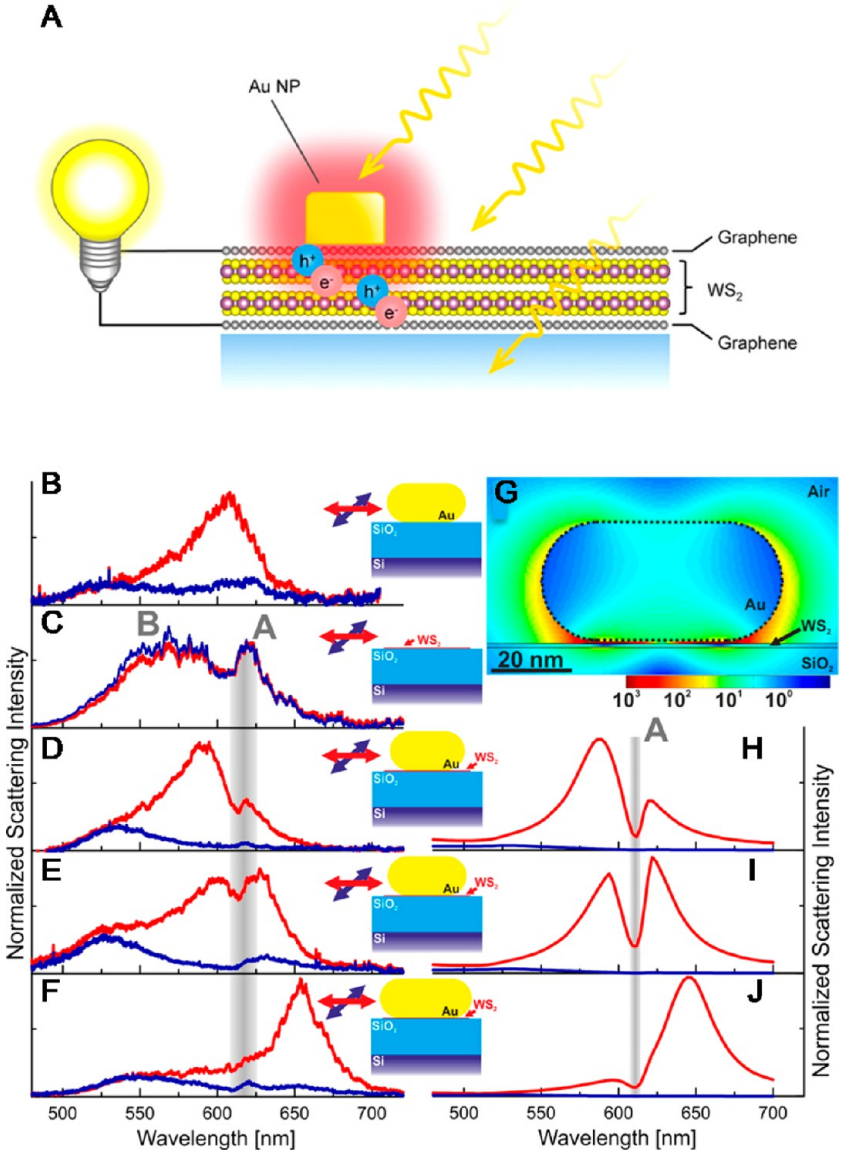

Figure 9. (A) Schematic illustration of a graphene/WS_2/graphene light-harvesting device. (B) Polarization-resolved scattering spectrum of a Au nanorod/SiO_2/Si. (C) Scattering spectrum of WS_2/SiO_2/Si. (D–F) Emission polarization-resolved scattering spectra of nanorods with different lengths on the WS_2/SiO_2/Si. (G) Calculated near-field intensity map at 612 nm wavelength. (H–J) Calculated emission polarization-resolved scattering spectra of nanorods with different lengths on the WS_2/SiO_2/Si.[82,83]

intervening oxide[60,61] or graphene layer[62] between the metal and MoS_2 can significantly weaken the Fermi level pinning and also reduce the contact resistance and SBH.

In addition to the modeling and macroscopic measurements of the contact resistance, material characterizations and localized investigations have also been carried out to probe the microscopic origins of the contact properties observed. Gong *et al.* studied the wetting and growth of nanometer thick evaporated Pd, Au, and Ag films on monolayer CVD MoS_2 using atomic force microscope (AFM) to image the metal film morphology and Raman spectra to monitor the MoS_2 monolayer quality.[63] Pd wets MoS_2 uniformly, while Au and Ag cluster on MoS_2. The metal clusters introduce local stress and strain at the metal/MoS_2 interface,[64] detrimental to the current injection and carrier transport. McDonnell *et al.* addressed the contact inhomogeneity issue in more detail using localized measurements, including *I*–*V* characteristics, X-ray photoelectron spectroscopy (XPS) core-level spectra, scanning tunneling microscopy (STM), and scanning tunneling spectroscopy (STS).[65] They found that the natural exfoliated MoS_2 has high intrinsic defect concentration, which imposes questions about the metal's influence on the MoS_2 electronic properties reported because, in those studies, MoS_2 is often assumed to be pristine and a perfect crystal.

In summary, the research on contact to 2D semiconductors is still in an early stage with much improvement of ρ_C required for decent device performance. MoO_x interlayer[66] or NO_2 surface doping[67] was shown to improve the contacts to MoS_2 and WSe_2, respectively. Reference 68 gives much information on the approaches that the research community has taken to search for better contacts in 2D FETs.

Contacting BP. BP, the bulk form of phosphorene, has attracted much attention because it has a narrow band gap in the range of 0.3–1.0 eV, tunable by the layer number and bridging the band gap between graphene (zero band gap) and TMDs (usually above 1 eV). Furthermore, it has high carrier

DOI: 10.1021/acsnano.6b01842
ACS Nano 2016, 10, 4895–4919

mobilities and demonstrates ambipolar transport, which opens up possibilities for complementary 2D semiconductor electronics. The electrical contacts to BP have been studied by researchers who have accumulated much knowledge in graphene and MoS_2 devices. Using TLM, Du *et al.* investigated Ni/Au (30/50 nm) and Pd/Au (30/70 nm) contacts on 18.7 nm exfoliated BP flakes.[69] For the high work function Pd (5.4 eV), $\rho_C = 3.15 \times 10^3\ \Omega{\cdot}\mu m$ and $L_T = 0.72\ \mu m$; for Ni with $\varphi_M = 5.0$ eV, $\rho_C = 1.75 \times 10^3\ \Omega{\cdot}\mu m$ and $L_T = 1.18\ \mu m$ at −40 V backgate. Because of the Schottky barrier formed between the contact and the BP, the device is, in fact, a Schottky barrier FET, similar to the case of MoS_2. Das *et al.*'s work[70] provides information on BP FET performance complementary to that of Du *et al.* using another high work function contact metal, Ti, with $\rho_C^{Ti} = 4.85 \times 10^3\ \Omega{\cdot}\mu m$. They also found that Fermi level pinning occurs at the metal/BP interface. More recently, Haratipour *et al.* reported $\rho_C = 1.14 \times 10^3\ \Omega{\cdot}\mu m$ on a ∼10 nm BP flake contacted with Ti/Au (5/100 nm), encapsulated by HfO_2.[71]

Parallel studies have also been conducted on BP. Anugrah *et al.* deposited ferromagnetic (FM) contacts on few-layer phosphorene and measured φ_{SB} of 110 and 200 meV for Py ($\varphi_M = 4.8$ eV) and Co ($\varphi_M = 5.0$ eV), respectively.[72] Similarly, TiO_2/Co contacts have also been applied to exfoliated few-layer BP and showed a reduction of the SBH from ∼206 meV for direct Co contact to <50 meV with TiO_2 tunneling layer, tunable by the backgate.

Applications. *Photodetection.* Tsai *et al.* demonstrated a Schottky metal−semiconductor−metal (MSM) photodetector using few-layer MoS_2 and interdigitated Au electrodes,[73] achieving a responsivity of 0.57 A/W at 532 nm wavelength with ∼70/110 μs rise/fall time. The device could endure a temperature of 200 °C, suitable for operation in harsh environments. The authors further improved the photodetector performance in a similar device by using trilayered MoS_2 and shrunken contact spacing,[74] demonstrating responsivity of ∼1.04 A/W, rise/fall time of 40/50 μs, and high radiation tolerance. Also in parallel with the work done on graphene,[43−45,75] Zhang *et al.* investigated the photovoltaic and the photothermoelectric contributions to the photocurrent generated in a MoS_2 Schottky barrier FET using scanning photocurrent microscopy.[76] Yu *et al.* demonstrated efficient gate-tunable photocurrent generation in a vertical junction of graphene−MoS_2−metal (Ti), utilizing the large junction area and the graphene as a work-function-tunable contact.[16] Cao and co-workers reported a GaSe MSM photodetector with high responsivity of 5000 A/W and response time of 10−20 ms.[77]

Zhang *et al.* fabricated phototransistors based on large-area WSe_2 monolayers contacted with the metals of different work functions.[78] It has been found that the low Schottky contact exhibits a very high photogain of $\sim 10^5$ and a specific detectivity of $\sim 10^{14}$ Jones, but the response time is ∼5 s. In contrast, the high Schottky contact shows a fast response time of ∼23 ms, but the photogain and specific detectivity decrease by several orders of magnitude. As the low work function of Ti is expected to decrease the contact resistance,[23] the interdigitated electrodes were employed to substantially increase the metal−MoS_2 contact region,[79] leading to the enhancement in photocarrier generation. A low contact resistance was achieved between MoS_2 and the Ti/Au electrodes with a responsivity of 2200 A/W under 532 nm illumination at an external bias of 1 V. The WSe_2-based devices fabricated by Liu *et al.* exhibit improved metal (In, Ag, Al, and Ti) contacts to WSe_2.[80] Device measurements supported by *ab initio* DFT calculations illustrate that the d-orbital of the contact metal plays a key role in forming low contact resistance with monolayer WSe_2. The In- and Ag-based contacts show the smallest contact resistance and the highest drive current.

It is known that light harvesting can be enhanced by the presence of metal NPs on 2D materials, inducing surface plasmon resonance.[81] As depicted in Figure 9A, a plasmonic Au NP traps the incident light through localized surface plasmon resonance and enhances exciton generation in its vicinity.[82] By coupling the 2D WS_2 to Au nanorods, Kern *et al.* significantly increased the light−matter interaction due to the plasmon resonance of the Au nanorod, which enhances the optical near-fields within the WS_2 monolayer, as illustrated in Figure 9B−J.[83] The photoluminescence intensity was increased by more than 1 order of magnitude. Butun *et al.* also achieved the enhancement of light emission from large-area monolayer MoS_2 using plasmonic silver nanodisc arrays, where enhanced photoluminescence up to 12-fold was obtained, as displayed in Figure 10A−D.[84]

Gas Sensing. Two-dimensional materials are of interest for gas sensors due to their high surface area, enhanced catalytic properties, active sites, reactivity, low power consumption, high process compatibility, and inherent flexibility.[85] MoS_2-,[86] WS_2-,[87] and SnS_2-[88]based materials have been fabricated for gas-sensing devices. Similar to graphene, the synergistic metal NPs in contact with 2D hybrid layers could also be employed to modulate the characteristics of gas sensors. As referred to as an electronic sensitization effect,[89] metal NPs are used to increase the overall active sensing surface area and the adsorption sites of gas molecules. The metals with high work function increase the hole concentration of the 2D material device. The Pd NP film contacted with MoS_2 has been found to enhance the gas response to NH_3.[48] Similar work was also reported in which metal oxide SnO_2 NPs induce a strong *p*-type doping effect for MoS_2.[47] However, low work function Al depletes the hole carriers of the device, thus leading to the increase of the sensitivity for detecting NO_2.

After Das *et al.* systematically investigated the ideal metal contact for the evaluation of intrinsic transport properties of MoS_2-based FETs,[23] Fang *et al.* found that degenerate vapor doping of the contact regions of WSe_2 FET devices could be effective in minimizing the Schottky barrier and lowering the contact resistance.[67,90] This was achieved by exposing the contact regions to NO_2 and K vapors, as displayed in Figure 11. By being exposed to the gas vapor, the barrier widths at the metal/2D materials' interfaces can be significantly reduced, leading to a more efficient carrier tunneling and lower resistance contacts. Liu *et al.* reported high-performance NO_2 (down to 20 ppb) and NH_3 (down to 1 ppm) sensing using CVD monolayer MoS_2 Schottky barrier FET,[91] elucidating the contribution of the Schottky barrier modulation upon analytical molecular adsorption in addition to the charge transfer mechanism in the channel. Although a BP device with similar structure was also reported for NO_2 sensing down to 5 ppb,[92] the authors deemed the effect of Schottky barrier modulation induced by NO_2 exposure minimal. Nonetheless, metals can be employed as a catalytic layer, which is generally deposited onto the surface of the 2D materials in the form of a thin film to enhance the decomposition of gas molecules. Alsaif *et al.* explained the H_2 gas reaction using the "hydrogen spillover effect".[93] The Au/Pd metal layer on the 2D MoO_3 induces the dissociation of H_2 molecules into electrons and H^+ ions. The

DOI: 10.1021/acsnano.6b01842
ACS Nano 2016, 10, 4895−4919

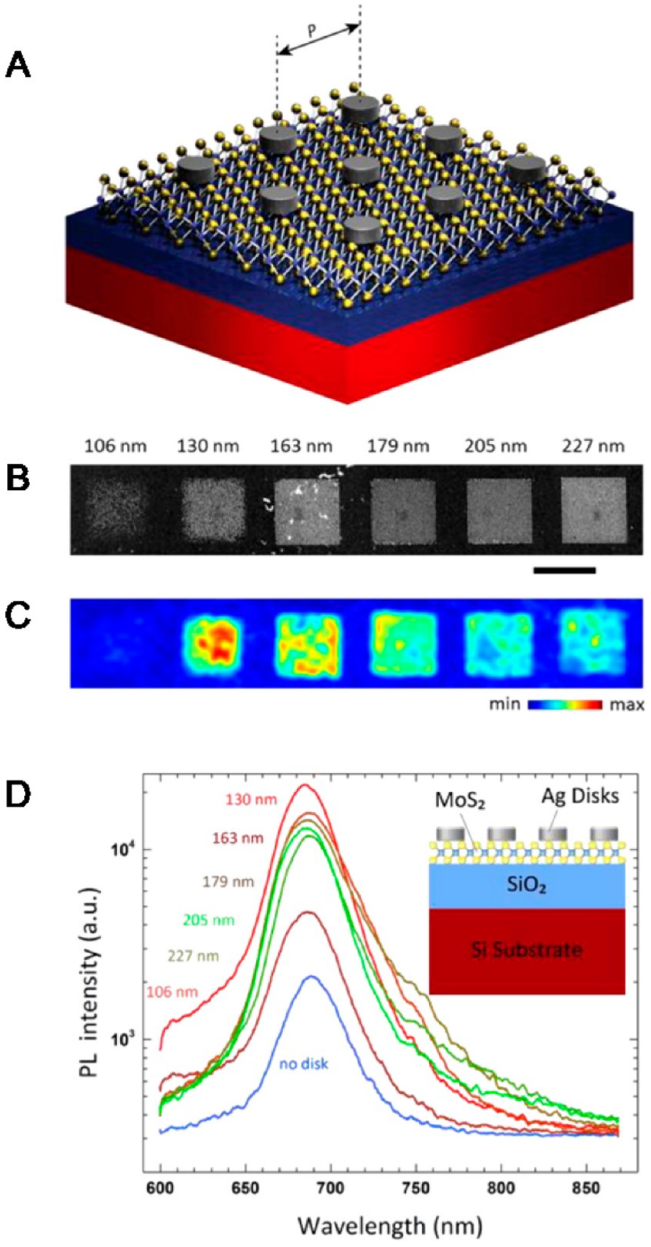

Figure 10. (A) Schematic illustration of the silver nanodisc array on MoS_2. (B) SEM image and (C) corresponding integrated photoluminescence map of the nanodisc arrays. (D) Photoluminescence spectra from the arrays.[84]

H^+ ions are transferred and reacted with O atoms in the first MoO_3 monolayer, forming OH_2 and H_xMoO_3. The rest of the H^+ ions then go underneath the MoO_3 layers.

Solar Cell. Shanmugam *et al.* demonstrated Schottky junction solar cells based on the stacked structure of ITO−CVD MoS_2−Au, operating in the spectral range of 350−950 nm,[94] with a power conversion efficiency of 0.7% for ∼110 nm thick MoS_2 membrane and 1.8% for ∼220 nm. Although there are a few other reports on utilizing 2D semiconductor devices for light harvesting,[95−97] they attribute most of the photovoltaic response to the 2D *p*−*n* junction instead of the metal−2D semiconductor Schottky junction.

GRAPHENE CONTACT TO CONVENTIONAL SEMICONDUCTORS

As a transparent semimetal, graphene has enormous potential in Schottky-junction-based optoelectronic applications when put in contact with conventional semiconductors, replacing normal metals. Considerable efforts have been devoted to understanding the fundamental properties of the graphene−3D semiconductor Schottky junction. In this section, we start with the basic 3D Schottky junction model, reviewing the experimental methods for extracting the Schottky junction parameters in graphene−conventional semiconductor junctions and looking at models proposed for this 2D metal−3D semiconductor system.

Schottky Junction: Barrier Height and Ideality Factor. Tongay *et al.* did the systematic study on graphite−conventional semiconductor contacts, providing foresight to the graphene−semiconductor junctions.[98] In this study, highly oriented pyrolytic graphite (HOPG) contacts were made to Si, GaAs, and SiC in "soft landing" forms: (1) spring-loaded bulk HOPG, where HOPG is gently pressed onto the substrate; (2) vdW adherence of cleaved HOPG flakes; and (3) HOPG "paint", which consists of graphite powder/flakes. All of these forms resulted in similar junction behavior. The junctions were characterized using the classical Schottky junction *I*−*V* and *C*−*V* characteristics. Under forward bias *V*, the current through the Schottky barrier is

$$I = I_S(T)\left[\exp\left(\frac{eV}{\eta k_B T}\right) - 1\right] \tag{9}$$

$$I_S(T) = AA^*T^2 \exp\left(-\frac{e\Phi_{B0}}{k_B T}\right) \tag{10}$$

where $I_S(T)$ is the saturation current under zero bias, A is the effective junction area, A^* is the Richardson constant of the semiconductor, and φ_{B0} is the zero-bias SBH. η is the ideality factor, which should be 1 if the Schottky junction current is purely from thermionic emission. Deviation of η from 1 could be due to bias-dependent SBH, generation recombination of the carriers, thermally assisted tunneling current, inhomogeneity of the junction, and image force lowering of the SBH. To exclude the extrinsic effects at the metal−semiconductor interface, the flat band zero-electric-field SBH φ_{BF} can be calculated as

$$\Phi_{BF} = \eta\Phi_{B0} - (\eta - 1)(k_B T/e)\ln(N_C/N_D) \tag{11}$$

where N_C is the effective DOS in the conduction band and N_D is the doping density. In addition to the forward *I*−*V* curve, φ_B could also be extracted from the *C*−*V* characteristics of the reverse-biased Schottky junction. The junction capacitance is

$$C_J = \sqrt{\frac{e\varepsilon_s N_D}{2(V_{bi} - V_R)}} \tag{12}$$

where ε_s is the dielectric constant of the semiconductor, N_D is the doping density, V_{bi} is the built-in potential, and V_R is the reverse-bias voltage. The barrier height is then $\varphi_{C-V} = V_{bi} + (E_C - E_F)$, where E_C is the conduction band bottom and E_F is the Fermi level. φ_{C-V} is often higher than φ_{B0} from the *I*−*V* curve and more closely related to φ_{BF}.

Figure 12 illustrates the extraction of the SBH φ_{B0} and the ideal factor η from the forward *I*−*V* curve of a graphene−Si Schottky junction.[99] From eq 9, we have

DOI: 10.1021/acsnano.6b01842
ACS Nano 2016, 10, 4895−4919

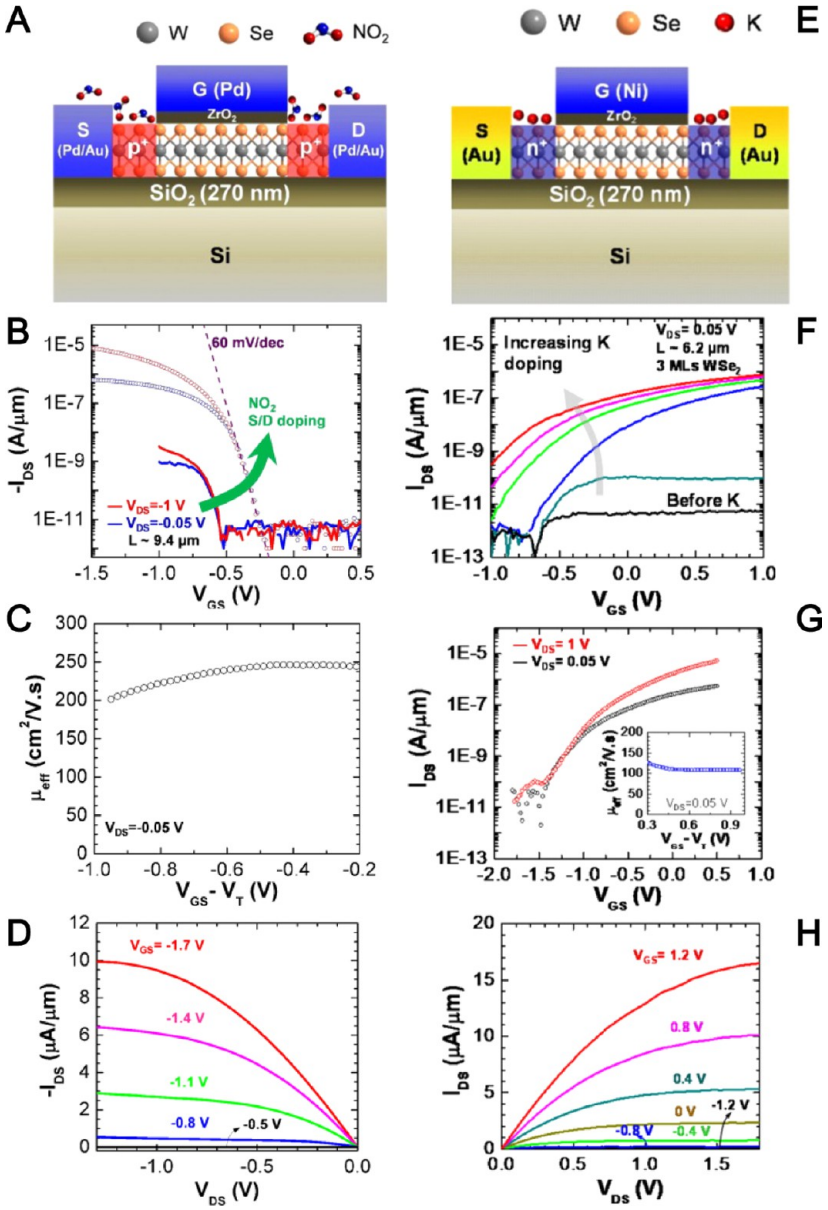

Figure 11. (A) Schematic illustration of NO_2 exposure inducing *p*-doped source/drain contacts of a WSe_2 FET. (B) Transfer characteristics of a device before and after NO_2 exposure. (C,D) Extracted effective hole mobility and output characteristics from the device in (B). (E) Schematic illustration of K exposure inducing *n*-doped source/drain contacts of a WSe_2 FET. (F) Transfer characteristics of a device before exposure and after 1, 20, 40, 70, and 120 min exposure. (G) Transfer characteristics of the device in (F) after 120 min exposure with extracted effective electron mobility displayed in the inset. (H) Output characteristics of the device in (F).[67,90]

$$\ln I \sim \frac{eV}{k_B \eta}\frac{1}{T} + \ln I_S(T) \tag{13}$$

The semilogarithmic plot of ln I *versus* $1/T$ yields a linear regime under moderate forward bias, where the series resistance of the Schottky diode has not emerged and the current can be described by eq 9. From the slope of the linear fit $eV/(k_B\eta)$, the ideality factor η of the Schottky diode can be extracted. The intercept of the fitted line at zero bias voltage yields the saturation current $I_S(T)$ (eq 10). At a given temperature, the zero-bias SBH φ_{B0} can be readily calculated, assuming that we have reliable values of the effective junction area A and the Richardson constant A^*. However, the accurate value of AA^* is not always available, and temperature-dependent measurement gives an alternative of obtaining φ_{B0}. From eq 10, we have

$$\ln\left(\frac{I_S(T)}{T^2}\right) = \ln(AA^*) - \left(\frac{e\Phi_{B0}}{k_B}\right)\frac{1}{T} \tag{14}$$

When $\ln(I_S(T)/T^2)$ *versus* $1/T$ is plotted, φ_{B0} is extracted from the linear fit slope; the intercept of the fitted line with the vertical coordinate also gives information about the junction area and the Richardson constant.

Figure 13 demonstrates the $C-V$ extraction of the SBH φ_{C-V}. According to eq 12, when $1/C^2$ *versus* V_R is plotted, the linear fit's slope gives the dopant density N_D, and the intercept with the horizontal axis gives the built-in potential V_{bi}, from which the SBH can be calculated as $\varphi_{C-V} = V_{bi} + (E_C - E_F)$. In addition to these routine methods of characterizing the Schottky junction properties, Yim *et al.* proposed a technique for extracting the junction resistance and capacitance using

DOI: 10.1021/acsnano.6b01842
ACS Nano 2016, 10, 4895−4919

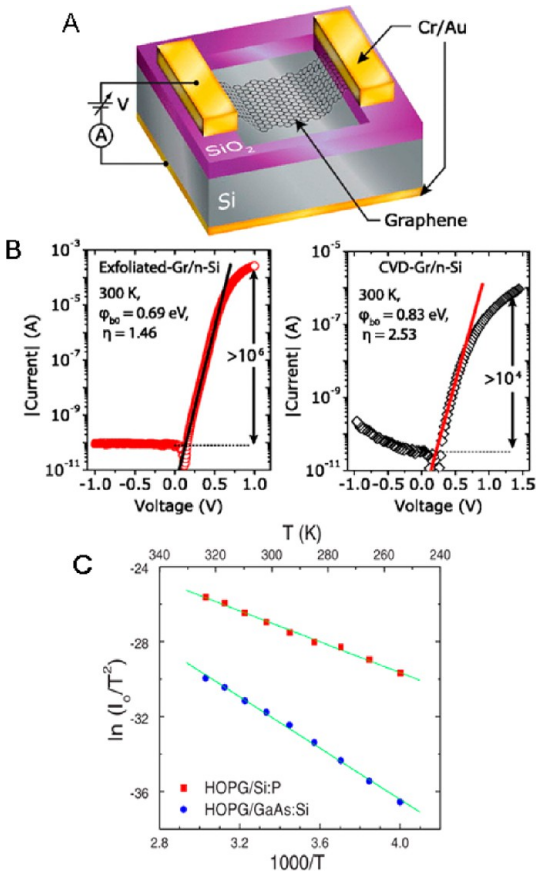

Figure 12. Extraction of the SBH and ideality factor η of the graphene/Si Schottky junction. (A) Device structure. (B) Linear fit of the forward $I-V$ curve according to the thermionic emission model. (C) Temperature dependence of the saturation current.[98,99]

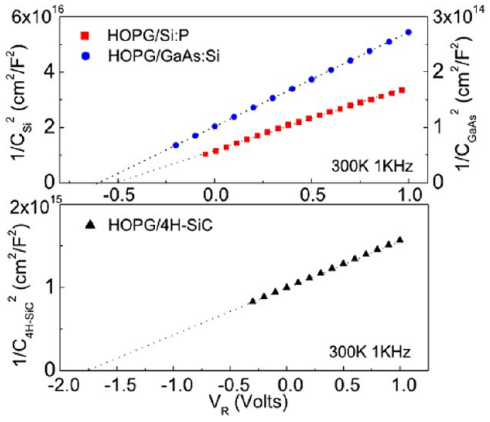

Figure 13. $C-V$ extraction of the SBH for Schottky junctions formed between graphite and Si, GaAs, and SiC.[98]

impedance spectroscopy,[100] which they suggested could differentiate the parasitic capacitance/resistance in the equivalent circuit of the device under testing. Here, the graphene-on-silicon Schottky device was divided into three parts, each having its own resistance and capacitance (Figure 14A). From the equivalent circuit, the total impedance of the device can be fitted to the experimental impedance spectrum (Figure 14B), and the fitting parameters give the individual R and C of the parts 1, 2, and 3 (Figure 14C). From the dependence of R and C on the bias voltage, the intrinsic junction component could

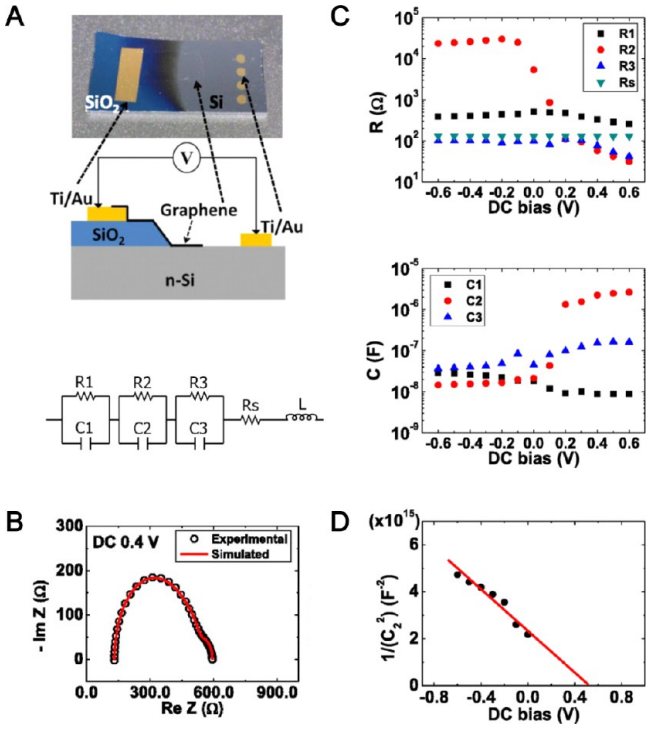

Figure 14. Extraction of the SBH using impedance spectroscopy. (A) Device layout and its equivalent circuit. (B) Measured impedance spectrum. (C) Fitting parameters (C and R of parts 1, 2, and 3) extracted from (B). (D) $C-V$ characteristics of part 2 for extracting the SBH.[100]

easily be identified. From the extracted capacitance value, the SBH was extracted using eq 15 (Figure 14D). This approach has already been used in a recent work for analyzing the graphene/silicon junction-based vapor sensing (chloroform, phenol, and methanol).[101]

Characterizing the Graphene/Conventional Semiconductor Junctions. As discussed above, the pioneering work of Tongay *et al.* adapted the classical Schottky junction model for the graphite/semiconductor contacts and suggested the possibilities of exploring and characterizing graphene/semiconductor systems using the well-established methods. Here we summarize the series of parallel studies done on graphene contacted to some most commonly used semiconductors, namely, on Si, Ge, GaAs, GaN, SiC, and ZnO (Table 3).

Silicon. Following Tongay's work, Chen *et al.* carried out the detailed study on the exfoliated bilayer graphene/silicon Schottky junction,[102] setting out the fundamentals for the future integration of graphene with silicon. Bilayer graphene on both n-type and p-type silicon substrates exhibited rectifying $I-V$ behavior, from which a SBH of 0.4 eV was extracted, consistent with ref 98. In this early work, however, the ideality factor η of the junctions was high, in the range of 4.89−7.69 for n-type Si and 29.67−33.50 for p-type Si. The photocurrent of the junctions was also characterized. To connect with our previous discussion of the contact resistance at the 2D/3D interface, this work gives a Au/graphene contact resistivity of 212×10^{-6} Ω·cm^2 and ρ_C at the graphene/Si interface is 73.6×10^{-6} Ω·cm^2, suggesting a bonding energy for graphene and Si higher than that with Au. After the initial graphite study,[98] Tongay *et al.* continued with a more systematic work on CVD graphene−semiconductor interfaces,[110] on n-type Si, GaAs, 4H-SiC, and GaN. Again, they used both $I-V$ and $C-V$

DOI: 10.1021/acsnano.6b01842
ACS Nano 2016, 10, 4895−4919

Table 3. Graphene/Conventional Semiconductor Schottky Junction Properties

3D semiconductor	Φ_{SB} (eV)	η	ref (year)	graphene type
n-Si	0.4	4.89−4.76	102 (2011)	mechanically exfoliated
p-Si	0.4	∼30	102 (2011)	mechanically exfoliated
GaN	0.74	2.9	103 (2011)	CVD
GaN	0.7	2.4	103 (2011)	CVD, *after anneal
AlGaN	0.4		104 (2014)	CVD
SiC	0.08		105 (2012)	epitaxial
SiC	0.58	4.5	106 (2014)	epitaxial
SiC	1.3		107 (2014)	CVD transferred on C−SiC
SiC	1.16		107 (2014)	CVD transferred on Si−SiC
SiC	0.85		108 (2009)	epitaxial, local *I*−*V*
SiC	0.36		108 (2009)	exfoliated then deposited, local *I*−*V*
ZnO	0.65	1.15	109 (2012)	CVD
IGZO	0.64 (off), 0.04 (on)	1.27	19 (2014)	CVD

characteristics to extract the Schottky junction parameters. The barrier height was rather different than the values reported before with exfoliated graphene, but the Schottky−Mott model holds well for all the systems measured. In this work, the authors pointed out an essential difference between graphene and a conventional metal is that the Fermi level shifts in graphene during the charge transfer across the graphene/semiconductor interface because of its low DOS. Moreover, a strong bias voltage also shifts the graphene Fermi level, which leads to significant changes in the diode current. Because of this tunability of the graphene Fermi level, the graphene/semiconductor junction properties could be adjusted by electric doping of the graphene layer. Yang *et al.* demonstrated this concept in their work,[111] as "graphene barrister" with a gate-controlled Schottky barrier at the graphene−silicon interface for achieving a current on/off ratio of 10^5. A similar idea was realized in ref 112 by controlling the graphene/silicon contact behavior (from Schottky to Ohmic) using a polymer electrolyte gate. The graphene doping tunes the graphene−silicon work function difference, leading to tunable photocurrent in the Schottky diode, as well. The model and experimental works on charge transfer at the graphene/semiconductor interface will be discussed in detail in another section.

Germanium. Excellent mobility was observed in graphene transferred onto the Ge substrate with GeO_x surface layers.[113] Baek *et al.* used graphene as a tunneling barrier between Ge and Co. The Ge/Co Schottky barrier could be tuned by the number of layers of the inserted graphene. Graphene here has potential as the tunneling barrier for spin injection from Co to Ge.[114]

Gallium Nitride. As a wide band gap (3.4 eV) semiconductor, GaN has been widely used in bright light-emitting diodes (LEDs). Its special properties lead to other applications in optoelectronics and high-power and high-frequency devices. Tongay *et al.* investigated the graphene/GaN junction properties at elevated temperatures to confirm the possibility of integrating graphene into GaN-based devices.[103] They found decent rectifying behavior in the as-fabricated junction, with φ_{B0} of 0.74 eV and η of 2.9. The rectification was preserved until 550 K and diminished above 650 K. After a 900 K anneal, the Schottky diode was improved with φ_{B0} of 0.70 eV and η of ∼2.4, possibly due to the reduction of impurities and residue at the interface. Graphene shows excellent thermal stability in this study, and the usual problem of interdiffusion of atoms at the metal/semiconductor interface in conventional Schottky junctions is avoided.

Alternatively, Shiu *et al.* used scanning photoelectron microscopy and high-resolution photoemission spectra to obtain the Schottky barrier properties at the graphene/GaN interface.[115] They demonstrated the visibility and the SBH of single-layer graphene on an *n*-type $GaN/AlN/Si_3N_4/Si(111)$ substrate and found that the SBH is decreased with decreasing numbers of layers of graphene. Therefore, monolayer graphene on GaN is most desirable for decreasing the barrier between the transparent electrode and GaN and improving the LED performance.

Silicon Carbide. Tadjer *et al.* investigated the Schottky junction formed between epitaxial graphene (EG) on SiC and the substrate,[105] using its *I*−*V* and *C*−*V* characteristics over a wide temperature range (15−320 K). Using TLM, they found the EG sheet resistance of 1408 Ω/sq and a contact resistivity of $3-7 \times 10^{-6}$ Ω·cm^2. The forward-bias barrier height was extracted to be 0.08 eV from the Richardson plot. Such a low barrier height was attributed to the image force decrease and maximized tunneling probability to the bottom of the SiC conduction band (field emission). From the temperature-dependent measurements, the Arrhenius behavior of the barrier height only persisted down to 140 K, and the ideality factor was almost temperature-independent, confirming again that the field emission was the dominant current component. The authors also determined the barrier height from the *C*−*V* characteristics to be 0.55−0.75 eV down to 80 K, which increased sharply to 1.09 eV at 15 K. The reverse-bias current increases significantly when the temperature decreases, while the forward-bias current does not show as strong a trend. The forward current is speculated to be dominated by defect-assisted tunneling. Dharmaraj *et al.* grew Bernal-stacked bilayer EG on 4H-SiC (0001) using low-energy e-beam irradiation, which breaks the bond in SiC and causes Si sublimation,[106] and observed the Schottky barrier formation and the rectification at the EG−SiC junction, with φ_{B0} ∼0.58 eV and η ∼4.5.

Zinc Oxide. Lee *et al.* fabricated Schottky junction sputtering ZnO on a prepatterned single-layer graphene sheet.[109] They measured φ_{B0} of 0.65 eV and an ideality factor η of 1.15. Using a backgate, the SBH can be modulated, which leads to improvement in the photoresponse of the device. Liu *et al.* fabricated gate-tunable graphene on indium gallium zinc oxide (IGZO) junction in vertical thin film transistors for potential applications in large-scale flexible electronics.[19] The Schottky junction had an ideality factor of 1.27 and barrier height of 640 meV in the off-state and 40 meV in the on-state with nearly linear Ohmic behavior.

DOI: 10.1021/acsnano.6b01842
ACS Nano 2016, 10, 4895−4919

Organic Crystals. The lack of knowledge of graphene contacting ultrathin organic thin films also prevents the development of organic electronics applications. Therefore, it is desirable to understand the intrinsic charge transport in the 2D limit between 2D materials such as graphene and organic crystals.[116] Generally, the charge transport occurs in the first few molecular layers near the dielectric interface assumed in organic FETs. Zhang *et al.* fabricated highly ordered single-crystalline mono- to tetralayer pentacene crystals on hexagonal boron nitride *via* vdW stacking.[117] They found that the charge transport is dominated by hopping in the first conductive layer and then transforms to band-like in subsequent layers due to strong modulation of the molecular packing by interfacial vdW interactions. Moreover, the structural modulation becomes negligible beyond the second conductive layer, leading to a mobility saturation thickness of ~3 nm. He *et al.* also grew few-layer dioctylbenzothienobenzothiophene (C(8)-BTBT) molecular crystals on a graphene/boron nitride substrate *via* vdW epitaxy with controlled thickness down to the monolayer.[118] The crystalline layers are atomically smooth and decoupled from the substrate due to weak vdW interactions, affording a pristine interface. A carrier mobility of 10 $cm^2\ V^{-1}\ s^{-1}$ and a saturation voltage of ~1 V have been achieved.

Junction Inhomogeneity. In most cases, the transferred graphene interacts with the substrate *via* weak vdW forces, and there could easily be wrinkles, folds, or defects in the graphene sheet, especially in CVD graphene. Even EG exhibits inhomogeneities. It has been discussed in previous sections that the ideality factor η of a graphene/semiconductor usually exceeds 1, suggesting inhomogeneity of the junction in addition to other possibilities such as tunneling current contribution. In this part, we will look into the experiments done at the nanoscale for localized $I-V$ characteristics, exploring spatially resolved Schottky junction properties.

Sonde *et al.* investigated the current distribution in graphene/SiC junctions using scanning current spectroscopy,[108] implementing Pt-coated conductive atomic force microscopy (CAFM), a technique developed by Giannazzo *et al.* for characterizing laterally inhomogeneous Schottky junctions in wide band gap semiconductors.[119] In this work, both EG and deposited/transferred graphene (DG) form Schottky contact with the single-crystalline SiC substrate. As shown in Figure 15, the local $I-V$ characteristics show distribution on both the SiC substrate and the graphene area, confirming the rectification yet inhomogeneous property of the junction. However, on the EG/SiC sample, at certain locations, the $I-V$ curve is linear, exhibiting Ohmic-like behavior. The histograms of the SBH give the same φ_{B0} of the Pt/SiC junction (~1.6 ± 0.2 eV), compared to φ_{B0} of DG/SiC ~ 0.85 ± 0.06 eV and φ_{B0} of EG/SiC ~ 0.36 ± 0.1 eV. It is interesting to note that the SiC substrate has such a high level of inhomogeneity when put into Schottky contact with the Pt-coated AFM tip. On the other hand, the DG demonstrates relatively high homogeneity in the contact, and the average SBH (~0.85 eV) is in reasonable agreement with the Mott–Schottky relation for graphene (W_{Gr} ~ 4.5 eV) and SiC (χ_{SiC} ~ 3.7 eV). The EG on SiC, however, experiences a Fermi level pinning ~0.49 eV above the Dirac point, due to the positively charged states at the interface between the Si face and C-rich reconstructed buffer layer during the epitaxial growth. From the $I-V$ characteristics, the energy distribution of these interface states is inhomogeneous and varies rapidly at the nanoscale.

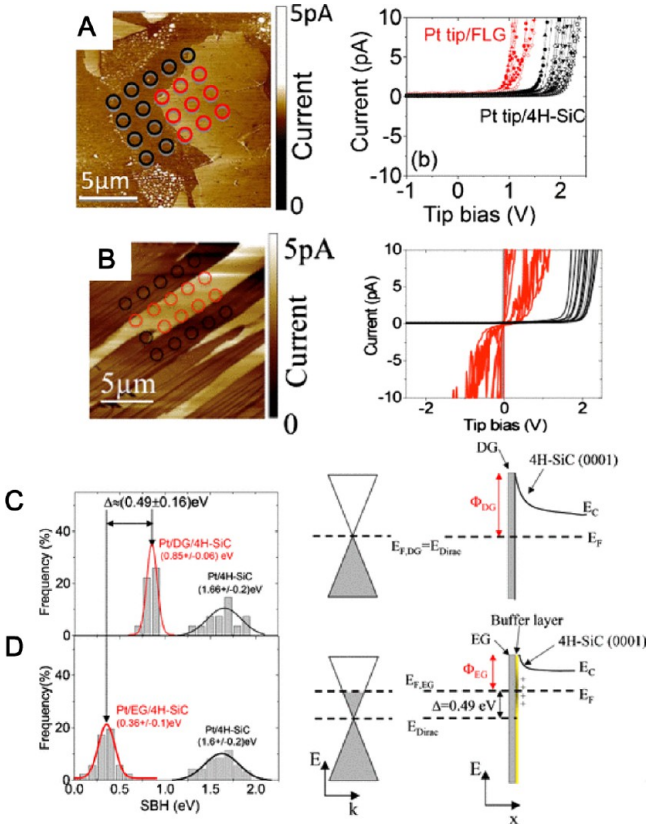

Figure 15. Inhomogeneity characterized by CAFM in graphene/SiC Schottky junctions. Sample topography and localized $I-V$ characteristics of (A) few-layer DG/SiC and (B) EG/SiC junctions. (C,D) Histograms and band diagrams for the sample in (A) and (B), respectively.[108]

AlGaN/GaN is also an important heterostructure for high-power electronics. Following up on the previous work of graphene/SiC junction inhomogeneities,[108] Giannazzo and co-workers investigated the graphene contact to AlGaN/GaN using the same methodology and found that the microstructure of the AlGaN layer plays a critical role in the junction nature of the contact, which could be either Schottky or Ohmic depending on the defects of the AlGaN layer.[104,120] For a perfect AlGaN layer contacted by the Au-coated conductive AFM tip, φ_{B0} ~ 0.9 eV and φ_{B0} ~ 0.6 eV for an AlGaN layer with V defects, due to preferential current paths at the defect locations. With graphene transferred on the AlGaN/GaN heterostructure, φ_{B0} for the perfect AlGaN sample was reduced to 0.4 eV, and for the V defect sample, the contact became Ohmic-like. Interestingly, the SBH exhibits much lower spread with the graphene compared with the bare CAFM tip/AlGaN/GaN contact. This effect was attributed to the current spreading/averaging effect of the graphene over the AlGaN surface.

Zhong *et al.* studied the electrical properties of the CVD graphene transferred onto both *n*- and *p*-GaN using conductive AFM and found that the wrinkles on graphene form Ohmic contact with the substrate while the flat regions are in Schottky contact with GaN.[121] Using density functional theory, they calculated the Fermi level at the standing and folded wrinkles of graphene, with zigzag or armchair directions. The local E_F shifts toward *n*- or *p*-type GaN for the two directions, respectively, acting as high-conductive channels.

DOI: 10.1021/acsnano.6b01842
ACS Nano 2016, 10, 4895–4919

Alternatively, Shivaraman *et al.* analyzed the inhomogeneity of the Schottky junction formed between EG and SiC using macroscopic characterizing methods, that is, the $I-V$ and $C-V$ measurements.[122] They based their analysis on the model proposed originally by Güttler[123] and Tung,[124] which suggests that φ_{B0} extracted from the $I-V$ curve is the effective barrier height and φ_{C-V} is the mean barrier height of the inhomogeneous junction. They satisfy the following relation

$$\Phi_{B0} = \Phi_{C-V} - \frac{q\sigma^2}{2k_BT} \tag{15}$$

where σ is the standard deviation of the Gaussian distribution and is assumed to be temperature-independent. This equation provides a means of extracting the spread of the barrier height distribution by plotting the difference between φ_{B0} and φ_{C-V} *versus* $1/T$. The standard deviation was found to be 137 ± 11 meV, in fair agreement with that in ref 108. Parui *et al.* characterized the Gaussian distribution of the SBH in graphene/*n*-Si diodes and found σ also in the range of ∼100 meV.[99]

Tomer *et al.* combine both the localized morphology/electrical measurements and macroscopic, temperature-dependent $I-V$ characteristics to study the intrinsic junction inhomogeneity of the transferred CVD graphene/SiC system.[107] Nonideal behaviors such as increasing φ_{B0} and decreasing η with increasing temperature are related to the spatial inhomogeneities in graphene, examined by STM and STS. STM/STS measurements over graphene ripples give a Fermi level shift of 270 meV with fwhm of 70 meV, with respect to the Dirac point. The SBH was measured to be 1.3 ± 0.18 eV and 1.16 ± 0.16 eV for graphene on C-terminated SiC and Si-terminated SiC, respectively. The spatial inhomogeneities are mostly due to ripples, ridges, and SiC steps, revealed by the STM, as shown in Figure 16.

Toward Low-Dimensional Models: Charge Transfer and Landauer Approach. As mentioned before, Tongay *et al.* proposed the model for charge transfer at the graphene/semiconductor interface, which is a significant difference between the role of graphene in a Schottky junction and that of a conventional metal, due to the low DOS near the Dirac point in graphene.[110] In contrast to a conventional Schottky diode, the reverse-bias current is not saturating but increasing continuously with the increased V_R (Figure 17). In the reverse-bias regime, the electron charge per unit area on the graphene is

$$Q = en_{induced} = C_J(V_{bi} + V_R) \tag{16}$$

where C_J is given by eq 12. When the residual doping carrier density n_0 in graphene is taken into account, the Fermi level shift with respect to the Dirac point can be calculated as

$$E_F = -\hbar|v_F|\sqrt{\pi\left(n_0 - \sqrt{\frac{\varepsilon_s N_D(V_{bi} + V_R)}{2e}}\right)} \tag{17}$$

Therefore, upon a reverse bias being applied, the SBH changes by the amount of

$$e\Delta\Phi_{SBH}(V_R) = -\Delta E_F(V_R) = \hbar v_F\left[\sqrt{\pi(n_0 - n_{induced})} - \sqrt{\pi n_0}\right]$$
$$\approx -\frac{1}{2}\hbar v_F\sqrt{\pi n_0}\frac{n_{induced}}{n_0} = -\frac{1}{2}\hbar v_F\sqrt{\frac{\pi\varepsilon_s N_D(V_{bi} + V_R)}{2en_0}} \tag{18}$$

Accordingly, the saturation current in a Schottky junction, given before in eq 10, becomes

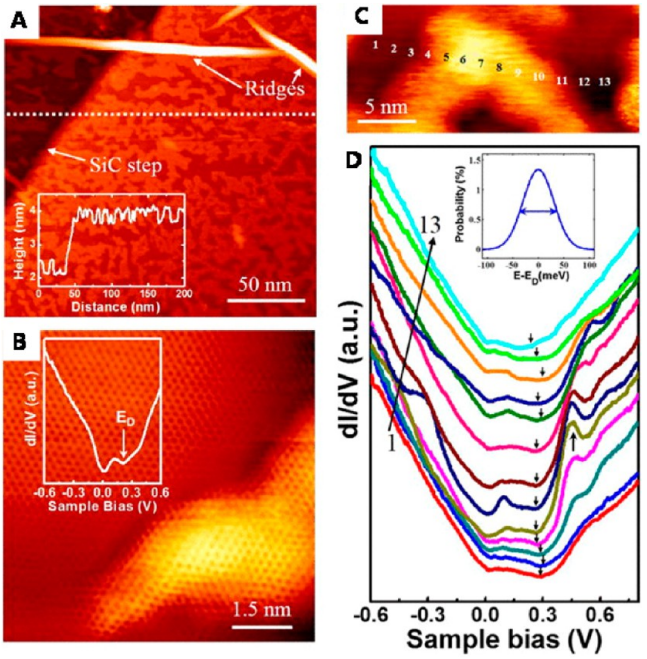

Figure 16. Inhomogeneities in a CVD graphene/SiC junction. (A) STM image of CVD graphene on SiC; inset is the profile along the dashed line. (B) STM image of the graphene ripples; inset shows the corresponding d*I*/d*V* spectrum. (C) STM image of a ripple. (D) d*I*/d*V* spectra taken from the corresponding spots shown in (C); normal probability distribution of the Dirac energy is shown in the inset.[107]

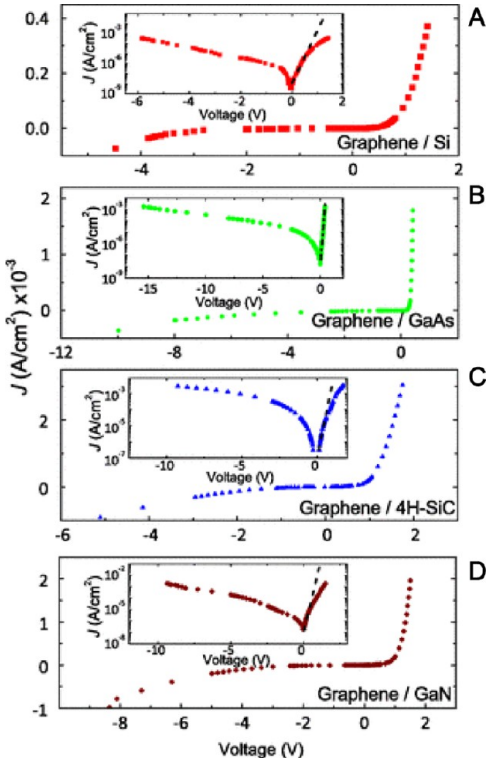

Figure 17. *J*–*V* characteristics at the graphene/(A) *n*-Si, (B) *n*-GaAs, (C) *n*-4H-SiC, and (D) *n*-GaN interfaces.[110]

$$I_S(T) = AA^*T^2\exp\left(-\frac{e\Phi^0_{SBH} + e\Delta\Phi_{SBH}(V)}{k_BT}\right) \tag{19}$$

DOI: 10.1021/acsnano.6b01842
ACS Nano 2016, 10, 4895–4919

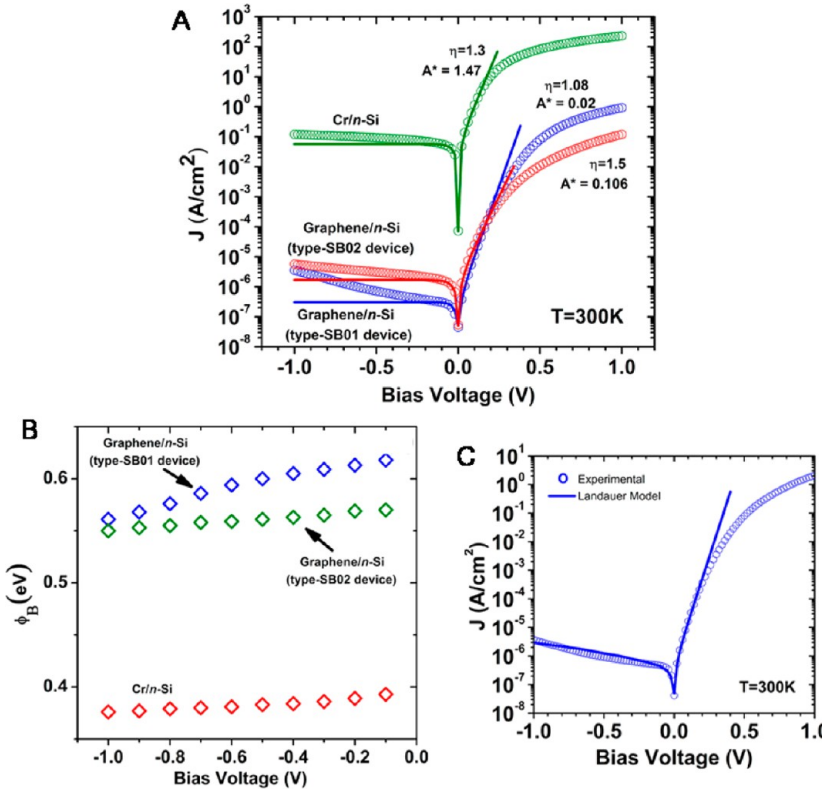

Figure 18. Schottky junction properties of a graphene/Si diode. (A) $I-V$ characteristics and the fit using classical thermionic emission model; A^* is the effective Richardson constant in $A{\cdot}cm^{-2}{\cdot}K^{-2}$. (B) SBH as a function of the reverse-bias voltage. (C) $I-V$ characteristics and the fit using the Landauer transport model.[126]

An *et al.* adapted this charge transfer model, as well, and calculated the bias-dependent Fermi level shift in a graphene/Si Schottky junction.[125] A systematic theoretical and experimental discussion about the charge transfer at the graphene/semiconductor interface could also be found in ref 121, with the experiment carried out in a graphene/GaN system. Cavallo *et al.* demonstrated an interesting result on enhanced carrier mobility in graphene deposited on a GeO_x/Ge substrate, due to the charge transfer between the surface states in GeO_x and the graphene.[113]

Finally, we will discuss the 2D nature of graphene as the "metal" part in a Schottky junction and its influence on the derivation of the junction current expression, compared with the classical Richardson form given by eqs 9 and 10. There is one recent discussion on the Landauer transport formalism in an "ideal" graphene−silicon junction.[126] Three kinds of samples were studied in this work: (1) CVD-grown graphene on Si; prior to the CVD growth, the surface of the Cu foil was treated by ammonium persulfate solution to etch away ∼700 nm of Cu, minimizing the metallic impurities in graphene. This kind of sample gave the most ideal Schottky junction behavior with $\eta \sim 1.08$, regularly CVD-grown graphene on Si with η of 1.63, and conventional metal/silicon Schottky junction Cr/Si with η of 1.3. The $J-V$ characteristics are shown in Figure 18A. The curious point is that while the classical Schottky junction model gives the Richardson constant for a certain semiconductor (Si in this study), the A^* extracted from the $J-V$ characteristics shows large variation in the three sets of devices. This discrepancy was explained by the Landauer transport formalism, as proposed by the authors. Instead of the Schottky junction current given by eqs 9 and 10, the Landauer formalism gives

$$J = \frac{e}{\tau}\int_{-\infty}^{+\infty} T(E)D(E)(f_g - f_{Si})\mathrm{d}E \tag{20}$$

where τ is the time scale for carrier injection from the contact, $T(E)$ is the transmission probability over the Schottky barrier φ_B, $D(E)$ is the graphene DOS given by $2/[\pi(h\nu_F)^2]|E| = D_0|E|$, where ν_F is the Fermi velocity, and f is the Fermi−Dirac distribution. Eq 20 yields

$$J = J_S\left[\exp\left(\frac{eV}{\eta k_B T}\right) - 1\right]$$
$$J_S = \left[\frac{eD_0}{\tau}(k_B T)^2\left(\frac{\Phi_B}{k_B T} + 1\right)\right]\exp\left(\frac{-\Phi}{k_B T}\right) \tag{21}$$

Comparing eq 21 with eq 10, it is therefore the graphene/semiconductor coupling time scale τ accounting for the low values of A^* obtained in the graphene Schottky junctions. τ is 4.62×10^{-11} s, as obtained from the fit. Figure 18B illustrates the reverse-bias-dependent barrier height φ_B observed in the "ideal" sets of graphene/Si samples, which is also in agreement with the charge transfer phenomenon discussed previously in this section. Using the Landauer formalism again

$$e\int_{-\infty}^{+\infty} D(E)f(E_f)\mathrm{d}E = C_{Si}|V| \tag{22}$$

the authors were able to fit the "ideal" junction $I-V$ behavior reasonably well, as shown in Figure 18C, accounting for the nonsaturating reverse-bias current.

DOI: 10.1021/acsnano.6b01842
ACS Nano 2016, 10, 4895−4919

Table 4. Graphene/3D Semiconductor Schottky Junction Photodetectors

material	responsivity	rise/fall time	wavelength (nm)	ref
Si	2.8 mA/W		1550	128
Si	29 mA/W	∼100 μs	850/940	129
Si	435 mA/W	a few milliseconds	850	130
Si	0.11 A/W		633	133
Si	300 V/W	0.5 s	550	133
Si	∼18−128 mA/W	0.26/0.54 ms	445	134
porous Si	0.2 A/W	3 μs	400	135
Ge	51.8 mA/W	23 μs	1400	127
GaAs	3.73 mA/W	72/122 μs	850	131
ZnO NW array	0.55 mV/W	0.1 s	1064	132
ZnO NW array	0.2 mV/W		808	132
ZnO NW array	0.32 mV/W		532	132
ZnO nanorod array	113 A/W	0.7/3.6 ms	365	136
Ge QD Gr/ZnO	9.7 A/W		1400	137

Applications. *Photodetectors.* Graphene/3D semiconductor Schottky junction has been broadly explored for photodetector applications. The device performances are summarized in Table 4.

Infrared Detection. Zeng *et al.* reported a monolayer graphene/Ge Schottky junction photodetector with a peak sensitivity at 1400 nm wavelength, with a responsivity of 51.8 mA/W and 23 μs response time.[127] The Stake group showed 2.8 mA/W responsivity at 1.55 μm wavelength using an exfoliated graphene/Si Schottky junction.[128] Lv *et al.* reported 29 mA/W, with ∼100 μs response time at 850/940 nm illumination with graphene/Si.[129] An *et al.* presented weak signal detectors using monolayer graphene/Si junctions with a photovoltage responsivity of $\sim 10^7$ V/W, a photocurrent responsivity up to 435 mA/W, and a microsecond response time.[130] These tunable and scalable devices are well-suited for broad-band (400−900 nm) photodetection, with responsivity peaking at 850 nm, ideal for low-power integrated optoelectronic circuit. Luo *et al.* used a GaAs nanocone array/monolayer graphene Schottky junction to detect near-infrared light, with a peak sensitivity of 3.73 mA/W at 850 nm illumination.[131] The rise/fall time is 72/122 μs. Liu *et al.* investigated the broad-band photoresponse of a ZnO nanowire array/reduced graphene oxide film photodetector under 1064, 808, and 532 nm illumination and achieved photovoltaic responsivity of 0.55, 0.20, and 0.33 mV/W, respectively,[132] with the photoresponse time of ∼0.1 s. Wang's group reported a high-performance Ge quantum dot decorated graphene/ZnO infrared photodetector.[137] The device demonstrated ∼9.7 A/W responsivity under 1400 nm illumination with a fast rise/fall time of ∼40/90 μs.

Visible Light. The MSM photodetector demonstrated by An *et al.* works at 633 nm wavelength with a responsivity of 0.11 A/W.[125] Zhang *et al.* introduced the direct growth of nanocrystalline graphene/graphite on Si/SiO_2 to form a metal-free Schottky junction,[133] which achieved a 300 V/W photovoltage responsivity with ∼0.5 s response time at 550 nm wavelength. Zhu *et al.* demonstrated that reduced graphene oxide/Si Schottky photodiodes showed responsivity in the range of 18.12−128.72 mA/W and rise/fall time of 0.26/0.54 ms under 445 nm light.[134]

Ultraviolet. Nie *et al.* presented the Schottky junction UV detector fabricated by coating a ZnO nanorod array with graphene.[136] The UV light is effectively trapped in the nanorod array, enhancing the absorption of the light, achieving a responsivity 113 A/W and the rise/fall time of 0.7/3.6 ms. Kim *et al.* reported near-UV detection using graphene/porous Si junctions,[135] with a responsivity of 0.2 A/W and ∼3 μs response time at 400 nm illumination.

Gas Sensors. Kim *et al.* reported Schottky diodes made from monolayer graphene on *p*- and *n*-Si substrates, exhibiting stable sensing ability to selected gas (NH_3) and aromatic molecules (anisole, benzene, chlorobenzene, and nitrobenzene), making them potentially useful for environmental and biocompatible sensors.[138] The sensing mechanism was attributed to the charge transfer from adsorbents to graphene, which directly affects the work function and conductivity of the graphene as well as the SBH. Uddin *et al.* demonstrated a H_2 sensor with down to sub-ppm sensitivity using a Pd- and Pt-functionalized graphene/Si heterostructure.[139] Under reverse bias, the junction current varies exponentially when the SBH changes due to the molecule adsorption, enabling low-power operation and tunable sensitivity. Singh *et al.* demonstrated NH_3 and NO_2 detection using the same device structure, confirming the SBH change using $C-V$ measurements.[140] Kim *et al.* fabricated Si nanowire arrays vertically aligned by metal-assisted chemical etching of the Si wafer. With graphene on top, the ends of the nanowires were prevented from being bundled and formed uniform Schottky junction with the graphene.[141] The device showed 37 and 1280% change in resistance and 3.5/0.15 and 12/0.15 s response/recovery time for O_2 and H_2 detection, respectively. Zhu *et al.* evaluated reduced graphene oxide/Si Schottky diodes for gas sensing, including CH_4, O_2, CO, NO_2, NO, and SO_2,[142] and discussed the influence of the oxygen functional groups on the surface of the reduced graphene oxide.

Solar Cells. The efficiencies of the graphene/3D semiconductor solar cells are summarized in Figure 19. Li *et al.* reported graphene/*n*-Si Schottky junction solar cells with efficiencies up to 1.5%.[143] The same group later demonstrated an enhanced efficiency of 2.86% using the Schottky junction formed between graphene and a Si nanowire array with faster response time.[144] Xie *et al.* also reported 2.15% efficiency using a similar device structure.[145] Feng *et al.* demonstrated up to 2.9% efficiency in graphene/silicon pillar array solar cells and enhanced it up to 4.35% after HNO_3 treatment.[146] Poly(3,4-ethylenedioxythiophene):polystyrenesulfonic acid (PEDOT:PSS) coating on graphene also improves the efficiency slightly.

DOI: 10.1021/acsnano.6b01842
ACS Nano 2016, 10, 4895−4919

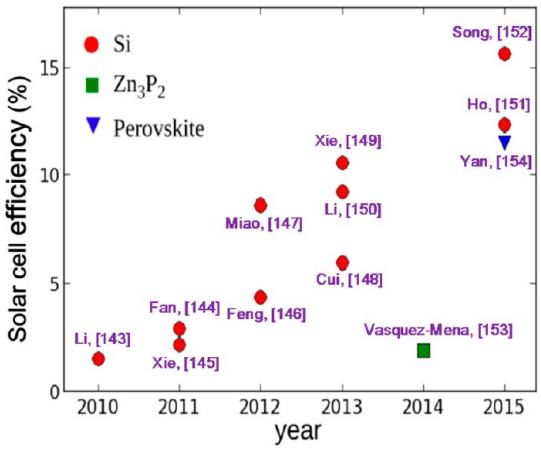

Figure 19. Efficiency of the graphene/3D semiconductor Schottky junction solar cells. The red dots are graphene/Si devices; the green square is graphene/Zn_3P_2; the blue triangle is graphene/CH_3NH_3I pasted perovskite. The numbers refer to the references.

Miao *et al.* improved the efficiency significantly to 8.6% using a graphene/*n*-Si Schottky junction with the graphene doped by bis(trifluoromethanesulfonyl)amide, which shifts the graphene chemical potential, and increased the carrier density and the built-in potential at the junction.[147] Cui *et al.* reported graphene/Si Schottky junction solar cells with initial efficiencies in the range of 1.94−2.66% and demonstrated an enhancement to 5.95% by doping treatment of $SOCl_2$.[148] The influence of other volatile oxidants such as HNO_3, HCl, and H_2O_2 was also investigated. Xie *et al.* carried out a study on the modification of the graphene/Si interface to tune the performance of the Schottky junction solar cell.[149] Methylated Si and the insertion of a thin P3HT organic layer at the junction interface suppressed the surface carrier recombination effectively and led to a high power conversion efficiency of 10.56%. Li *et al.* demonstrated an efficiency of 9.2% by nitrate ion doping of a graphene/*n*-Si solar cell.[150] Ho *et al.* reported the selective filling of the topological cracks in graphene using Au NPs in a graphene/Si Schottky junction solar cell[151] and achieved an efficiency as high as 12.3%. Song *et al.* investigated the influence of the native oxide at the graphene/Si junction interface and selected the optimal oxide thickness for efficiency enhancement.[152] When the graphene was doped with $AuCl_3$ and coated with a TiO_2 antireflective layer, the efficiency was improved to 15.6%.

Vazquez-Mena *et al.* presented a graphene/Zn_3P_2 solar cell with gate-tunable junction barrier[153] and showed an efficiency of 1.9% with an open-circuit voltage of 0.53 V. Yan *et al.* reported 11.5% efficiency in the device formed using multilayer graphene and CH_3NH_3I pasted onto perovskite.[154]

TWO-DIMENSIONAL SEMICONDUCTOR CONTACT TO CONVENTIONAL SEMICONDUCTORS: THE *p*−*n* JUNCTION

The integration of 2D semiconductors onto 3D semiconductor substrates opens up possibilities of device design for current rectification, photodetection, and energy harvesting. The layered semiconductors such as TMDs (*e.g.*, MoS_2) typically do not have out-of-plane bonds at the surface, therefore diminishing lattice mismatch and stress/strain-related problems at the heterojunction interface.

Lee *et al.* grew MoS_2 directly on SiC using CVD and characterized the *p*−*n* junction formed between the 2D MoS_2 and 3D SiC.[155] Figure 20 demonstrates the *I*−*V* and *C*−*V*

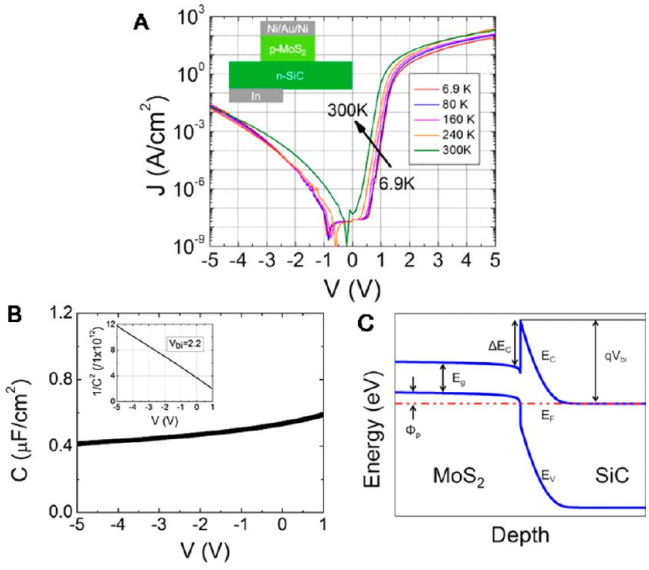

Figure 20. Properties of a *p*-MoS_2/*n*-SiC junction. (A) Temperature-dependent *I*−*V* characteristics; inset shows the device structure. (B) *C*−*V* characteristics; inset is the linear $1/C^2$ plot for extracting the built-in voltage. (C) Band diagram.[155]

characteristics. The *I*−*V* curve does not show strong temperature dependence and follows the multistep recombination tunneling current expression, giving an ideality factor η of 2.1. Chuang *et al.* demonstrated nearly ideal electrical properties of the InAs/WSe_2 junction with an ideality factor of 1.1.[156]

Yim *et al.* investigated photodiodes consisting of CVD MoS_2 (*n*-type) and *p*-type silicon (Figure 21A).[157] They varied the thickness of the MoS_2 layer in the range of ∼4−16 nm. All of the devices showed current rectification and broad spectrum photoresponse. The photocurrent exhibited strong dependence on the MoS_2 thickness (Figure 21B). The large photocurrent at higher MoS_2 thickness is probably due to the enhanced light absorption volume in thicker MoS_2 films. Esmaeili-Rad *et al.* reported the integration of 60 nm mechanically exfoliated MoS_2 onto a thin film amorphous silicon (a-Si, 100 nm) MSM structure (Figure 21C), which enhances the performance of the original a-Si photodetector.[158] Amorphous Si has a low mobility (∼10 $cm^2\ V^{-1}\ s^{-1}$), and the integration of MoS_2 makes the device 10× faster with the photocurrent rise/fall time of ∼0.3 ms and responsivity of 210 mA/W at 550 nm wavelength. Li *et al.* also investigated the photodiodes formed between exfoliated monolayer MoS_2 and both *n*- and *p*-type silicon[159] and achieved a high photoresponse of 7.2 A/W in the MoS_2/*n*-Si heterostructure. MoS_2/*p*-Si demonstrated a weaker built-in voltage. Lopez-Sanchez *et al.* demonstrated both LEDs and solar cells with the *n*-type exfoliated monolayer MoS_2/*p*-Si heterojunction.[161] The LED shows a low threshold power density of 3.2 W/cm^2, significantly lower than previously reported 15 kW/cm^2 for other MoS_2 electroluminescent devices. The solar cell has an external quantum efficiency of 4.4%. Tsai *et al.* fabricated solar cells using CVD monolayer MoS_2 transferred to *p*-Si.[162] The built-in electric field at the MoS_2/*p*-Si interface separates the photogenerated carriers and produces a photocurrent or open-circuit current. In this work,

DOI: 10.1021/acsnano.6b01842
ACS Nano 2016, 10, 4895−4919

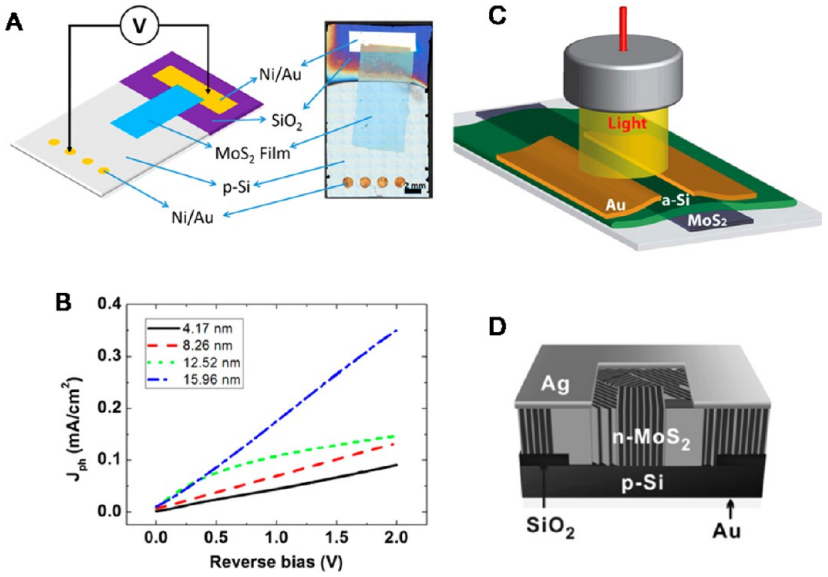

Figure 21. (A) Schematic diagram and photograph of the MoS_2/Si photodiode. (B) MoS_2 thickness dependence of the photocurrent density for devices shown in (A). (C) Schematic illustration of the Si/MoS_2 MSM photodetector. (D) Schematic of the MoS_2/Si photodetector, showing the vertically standing layered MoS_2.[157,158,160]

the MoS_2/*p*-Si device shows a power conversion efficiency of 5.23%, reported to be the highest among all monolayer TMD solar cells. Hao *et al.* deposited bulk-like MoS_2 film on the *p*-Si substrate using dc magnetron sputtering to form MoS_2/Si *p*−*n* junctions.[163] Current rectification and photovoltaic characteristics were also observed in these devices. Wang *et al.* demonstrated the sputtering deposition of MoS_2 films with a vertically standing layered structure on *p*-Si,[160] as shown in Figure 21D. The junction showed an on/off ratio of 5000 and ideality factor of 1.83. As a photodiode, the heterostructure has a high detectivity of ~10^{13} Jones and short response time of ~3 μs, due to the special vertically standing layered MoS_2 which offers strong light absorption and fast photogenerated carrier separation and transport.

PERSPECTIVE

Two-dimensional electronics has become an extremely active field over the past 10 years, with intriguing expectations for real-life applications in the foreseeable future and eventually bringing about the ultimate flexible electronics. In this roadmap, integrating the 2D materials with existing 3D CMOS technology is the low-hanging fruit, and indeed, there have already been devices commercialized, such as graphene touch screen, graphene-coated LEDs, *etc.* However, in these initial products, the outstanding electrical properties of graphene are implemented only to a limited extent. The TMD devices are still far away from applications because of their relatively poor performance and the challenges in large-scale reproducible production. BP and X-enes[164,165] are expected to offer relatively high mobility and a tunable band gap but suffer from ambient instability, and their investigations are still at an early stage. Two-dimensional molecular crystals held by vdW forces, which could effectively eliminate interlayer screening, leading to directly probing disorder effects and interfaces on charge transport, have barely been studied. The understanding of the contact with these 2D molecular crystals would make the carrier injection and modulation more efficient to improve the performance of organic FETs. However, the fundamental issues regarding the nature of charge transport in the 2D organics have not been addressed.

For any of the 2D materials discussed, making the electrical contact is the prerequisite for any kind of research or application, especially for high-performance electronic or optoelectronic devices. From this review, we see that the contact to graphene has improved from $\rho_C \sim 10^{-4}$ to 10^{-5} Ω·cm^2 around 2010 to the current state-of-art of ~10^{-8} to 10^{-9} Ω·cm^2 in most recent studies, by introducing well-controlled graphene edges in the contact area and using metals which form carbides with graphene. In first section of this review, mechanically exfoliated and CVD graphene devices are discussed in detail for high-performance applications. On the other hand, liquid exfoliated graphene or solution-processable layered materials are more important in large-scale production of thin film transistors aiming at lower-performance electronics.[5,166] Though there are some encouraging results on ink-printed electronics,[167−171] the contact to the conductive ink has not been sufficiently studied, which remains a blank to be filled in. TMDs and BP lag behind graphene by about 4 orders of magnitude in terms of the contact resistivity, and the microscopic mechanisms of contact formation between metal and 2D semiconductors are still not well understood. Graphene with etched edges could serve as the buffer layer between the 2D semiconductor and the metal for contact improvement.[172] Alternatively, the 1T metallic phase in TMDs is explored for Ohmic contact with the metal electrodes, while the TMD channel is maintained at the regular 2H phase.[173−176] FETs with 1T phase/metal contacts are reported to show superior mobilities and contact resistivity as low as 200−300 Ω·μm for MoS_2.[175] TMDs and BP have large spin−orbit coupling and are attractive candidates for spin manipulation in hybrid ferromagnetic systems. The very young field of using ferromagnetic metal contact for spin-polarized current injection has only seen a few published works merely characterizing the Schottky junction barrier height, tunable by inserting a tunnel barrier, yet not concerning the spins. Much more work is needed for injecting spins into these 2D semiconductors.

DOI: 10.1021/acsnano.6b01842
ACS Nano 2016, 10, 4895−4919

Contacting graphene or 2D semiconductors to 3D semiconductors provides alternative routes for making diodes. Most of metal/2D materials are Schottky contacts, which lead to the measured two-point resistance from TLM depending on the voltage bias and polarization. Most of the works applied to TLM roughly estimate contact resistance of 2D materials. Few works thoroughly studied this limitation. Very similar to the contact resistance problem, the fundamental issue in these 2D/3D systems is the transport of the carriers between 2D and 3D systems. Although the physical picture is completely different from a 3D/3D interface, the research community has been using the conventional models for years. This approach is apparently problematic, as many of the parameters would have questionable physical meaning, such as the Richardson constant in a Schottky diode. An understanding of the 2D/3D heterojunction transport is necessary and in urgent need for either the fundamental device physics or the improvement of the device performance.

AUTHOR INFORMATION

Corresponding Author

*E-mail: yangxu-isee@zju.edu.cn.

Author Contributions

⊥Y.X. and C.C. contributed equally to this work.

Notes

The authors declare no competing financial interest.

ACKNOWLEDGMENTS

The authors thank Prof. Kostya Novoselov, Prof. Wencai Ren, Prof. Manish Chhowalla, Prof. Zhongze Gu, Prof. Liwei Liu, Prof. Xinran Wang, and Dr. Yuan Liu for helpful discussion and comments. This work is supported by the National Science Foundation (DMR1508144), NSFC (Grant Nos. 61274123 and 61474099), micro/nano-fabrication platform of ZJU University, and the Fundamental Research Funds for the Central Universities (2016XZZX001-05). This work is also supported by ZJU Cyber Scholarship and Cyrus Tang Center for Sensor Materials and Applications, the Open Research Fund of State Key Laboratory of Bioelectronics, Southeast University, the Open Research Fund of State Key Laboratory of Nanodevices and Applications at Chinese Academy of Sciences (No. 14ZS01), and Visiting-by-Fellowship of Churchill College at the University of Cambridge.

VOCABULARY

contact resistance, resistance due to the contacting of the materials interfaces; an inherent property which is independent of the measuring approach; **transfer length method**, the contact resistance measuring method, in which the resistors of several different lengths are constructed; with measured the total resistances, the contact resistance can be extracted by extrapolating back to the resistor length at zero; **Schottky junction**, the boundary between a metal and semiconductor exhibiting rectifying characteristics; **Schottky barrier height**, the potential energy barrier for electrons formed at the Schottky junction; **ideality factor**, a parameter equals between 1 and 2, representing the ratio between diffusion and recombination current, indicating the number of defects in the barrier region; **Ohmic contact**, a nonrectifying electrical junction that exhibits a linear current−voltage curve as with Ohm's law; ***p*−*n* heterojunctions**, the boundary between *p*-type and *n*-type semiconductor materials

REFERENCES

(1) Ferrari, A. C.; Bonaccorso, F.; Fal'ko, V.; Novoselov, K. S.; Roche, S.; Boggild, P.; Borini, S.; Koppens, F. H. L.; Palermo, V.; Pugno, N.; Garrido, J. A.; Sordan, R.; Bianco, A.; Ballerini, L.; Prato, M.; Lidorikis, E.; Kivioja, J.; Marinelli, C.; Ryhanen, T.; Morpurgo, A.; et al. Science and Technology Roadmap for Graphene, Related Two-Dimensional Crystals, and Hybrid Systems. *Nanoscale* **2015**, *7*, 4598−4810.

(2) Fiori, G.; Bonaccorso, F.; Iannaccone, G.; Palacios, T.; Neumaier, D.; Seabaugh, A.; Banerjee, S. K.; Colombo, L. Electronics Based on Two-Dimensional Materials. *Nat. Nanotechnol.* **2014**, *9*, 768−779.

(3) Koppens, F. H. L.; Mueller, T.; Avouris, P.; Ferrari, A. C.; Vitiello, M. S.; Polini, M. Photodetectors Based on Graphene, Other Two-Dimensional Materials and Hybrid Systems. *Nat. Nanotechnol.* **2014**, *9*, 780−793.

(4) Butler, S. Z.; Hollen, S. M.; Cao, L.; Cui, Y.; Gupta, J. A.; Gutiérrez, H. R.; Heinz, T. F.; Hong, S. S.; Huang, J.; Ismach, A. F.; Johnston-Halperin, E.; Kuno, M.; Plashnitsa, V. V.; Robinson, R. D.; Ruoff, R. S.; Salahuddin, S.; Shan, J.; Shi, L.; Spencer, M. G.; Terrones, M.; et al. Progress, Challenges, and Opportunities in Two-Dimensional Materials Beyond Graphene. *ACS Nano* **2013**, *7*, 2898−2926.

(5) Franklin, A. D. Nanomaterials in Transistors: From High-Performance to Thin-Film Applications. *Science* **2015**, *349*, aab2750.

(6) Xia, F.; Wang, H.; Xiao, D.; Dubey, M.; Ramasubramaniam, A. Two-Dimensional Material Nanophotonics. *Nat. Photonics* **2014**, *8*, 899−907.

(7) Kim, K.; Choi, J.-Y.; Kim, T.; Cho, S.-H.; Chung, H.-J. A Role for Graphene in Silicon-Based Semiconductor Devices. *Nature* **2011**, *479*, 338−344.

(8) Novoselov, K. S.; Fal'ko, V. I.; Colombo, L.; Gellert, P. R.; Schwab, M. G.; Kim, K. A Roadmap for Graphene. *Nature* **2012**, *490*, 192−200.

(9) Liao, L.; Duan, X. Graphene for Radio Frequency Electronics. *Mater. Today* **2012**, *15*, 328−338.

(10) Weiss, N. O.; Zhou, H.; Liao, L.; Liu, Y.; Jiang, S.; Huang, Y.; Duan, X. Graphene: An Emerging Electronic Material. *Adv. Mater.* **2012**, *24*, 5782−5825.

(11) Wang, Q. H.; Kalantar-Zadeh, K.; Kis, A.; Coleman, J. N.; Strano, M. S. Electronics and Optoelectronics of Two-Dimensional Transition Metal Dichalcogenides. *Nat. Nanotechnol.* **2012**, *7*, 699−712.

(12) Jariwala, D.; Sangwan, V. K.; Lauhon, L. J.; Marks, T. J.; Hersam, M. C. Emerging Device Applications for Semiconducting Two-Dimensional Transition Metal Dichalcogenides. *ACS Nano* **2014**, *8*, 1102−1120.

(13) Geim, A. K.; Grigorieva, I. V. Van Der Waals Heterostructures. *Nature* **2013**, *499*, 419−425.

(14) Wang, H.; Liu, F.; Fu, W.; Fang, Z.; Zhou, W.; Liu, Z. Two-Dimensional Heterostructures: Fabrication, Characterization, and Application. *Nanoscale* **2014**, *6*, 12250−12272.

(15) Yu, W. J.; Li, Z.; Zhou, H.; Chen, Y.; Wang, Y.; Huang, Y.; Duan, X. Vertically Stacked Multi-Heterostructures of Layered Materials for Logic Transistors and Complementary Inverters. *Nat. Mater.* **2013**, *12*, 246−252.

(16) Yu, W. J.; Liu, Y.; Zhou, H.; Yin, A.; Li, Z.; Huang, Y.; Duan, X. Highly Efficient Gate-Tunable Photocurrent Generation in Vertical Heterostructures of Layered Materials. *Nat. Nanotechnol.* **2013**, *8*, 952−958.

(17) Akinwande, D.; Petrone, N.; Hone, J. Two-Dimensional Flexible Nanoelectronics. *Nat. Commun.* **2014**, *5*, 5678.

(18) Chae, S. H.; Yu, W. J.; Bae, J. J.; Duong, D. L.; Perello, D.; Jeong, H. Y.; Ta, Q. H.; Ly, T. H.; Vu, Q. A.; Yun, M.; Duan, X.; Lee, Y. H. Transferred Wrinkled Al_2O_3 for Highly Stretchable and Transparent Graphene−Carbon Nanotube Transistors. *Nat. Mater.* **2013**, *12*, 403−409.

(19) Liu, Y.; Zhou, H.; Cheng, R.; Yu, W.; Huang, Y.; Duan, X. Highly Flexible Electronics from Scalable Vertical Thin Film Transistors. *Nano Lett.* **2014**, *14*, 1413−1418.

DOI: 10.1021/acsnano.6b01842
ACS Nano 2016, 10, 4895−4919

(20) Cheng, R.; Jiang, S.; Chen, Y.; Liu, Y.; Weiss, N.; Cheng, H.-C.; Wu, H.; Huang, Y.; Duan, X. Few-Layer Molybdenum Disulfide Transistors and Circuits for High-Speed Flexible Electronics. *Nat. Commun.* **2014**, *5*, 5143.
(21) Tomanek, D. Interfacing Graphene and Related 2D Materials with the 3D World. *J. Phys.: Condens. Matter* **2015**, *27*, 133203.
(22) Allain, A.; Kang, J.; Banerjee, K.; Kis, A. Electrical Contacts to Two-Dimensional Semiconductors. *Nat. Mater.* **2015**, *14*, 1195−1205.
(23) Das, S.; Chen, H.-Y.; Penumatcha, A. V.; Appenzeller, J. High Performance Multilayer MoS_2 Transistors with Scandium Contacts. *Nano Lett.* **2013**, *13*, 100−105.
(24) Radisavljevic, B.; Radenovic, A.; Brivio, J.; Giacometti, V.; Kis, A. Single-Layer MoS_2 Transistors. *Nat. Nanotechnol.* **2011**, *6*, 147−150.
(25) Bai, J.; Liao, L.; Zhou, H.; Cheng, R.; Liu, L.; Huang, Y.; Duan, X. Top-Gated Chemical Vapor Deposition Grown Graphene Transistors with Current Saturation. *Nano Lett.* **2011**, *11*, 2555−2559.
(26) Novoselov, K. S.; Geim, A. K.; Morozov, S. V.; Jiang, D.; Zhang, Y.; Dubonos, S. V.; Grigorieva, I. V.; Firsov, A. A. Electric Field Effect in Atomically Thin Carbon Films. *Science* **2004**, *306*, 666−669.
(27) Venugopal, A.; Colombo, L.; Vogel, E. M. Contact Resistance in Few and Multilayer Graphene Devices. *Appl. Phys. Lett.* **2010**, *96*, 013512.
(28) Nagashio, K.; Nishimura, T.; Kita, K.; Toriumi, A. Contact Resistivity and Current Flow Path at Metal/Graphene Contact. *Appl. Phys. Lett.* **2010**, *97*, 143514.
(29) Robinson, J. A.; LaBella, M.; Zhu, M.; Hollander, M.; Kasarda, R.; Hughes, Z.; Trumbull, K.; Cavalero, R.; Snyder, D. Contacting Graphene. *Appl. Phys. Lett.* **2011**, *98*, 053103.
(30) Moon, J. S.; Antcliffe, M.; Seo, H. C.; Curtis, D.; Lin, S.; Schmitz, A.; Milosavljevic, I.; Kiselev, A. A.; Ross, R. S.; Gaskill, D. K.; Campbell, P. M.; Fitch, R. C.; Lee, K.-M.; Asbeck, P. Ultra-Low Resistance Ohmic Contacts in Graphene Field Effect Transistors. *Appl. Phys. Lett.* **2012**, *100*, 203512.
(31) Giovannetti, G.; Khomyakov, P. A.; Brocks, G.; Karpan, V. M.; van den Brink, J.; Kelly, P. J. Doping Graphene with Metal Contacts. *Phys. Rev. Lett.* **2008**, *101*, 026803.
(32) Xia, F.; Perebeinos, V.; Lin, Y.-m.; Wu, Y.; Avouris, P. The Origins and Limits of Metal-Graphene Junction Resistance. *Nat. Nanotechnol.* **2011**, *6*, 179−184.
(33) Sui, Y.; Appenzeller, J. Screening and Interlayer Coupling in Multilayer Graphene Field-Effect Transistors. *Nano Lett.* **2009**, *9*, 2973−2977.
(34) Wang, L.; Meric, I.; Huang, P. Y.; Gao, Q.; Gao, Y.; Tran, H.; Taniguchi, T.; Watanabe, K.; Campos, L. M.; Muller, D. A.; Guo, J.; Kim, P.; Hone, J.; Shepard, K. L.; Dean, C. R. One-Dimensional Electrical Contact to a Two-Dimensional Material. *Science* **2013**, *342*, 614−617.
(35) Smith, J. T.; Franklin, A. D.; Farmer, D. B.; Dimitrakopoulos, C. D. Reducing Contact Resistance in Graphene Devices through Contact Area Patterning. *ACS Nano* **2013**, *7*, 3661−3667.
(36) Leong, W. S.; Gong, H.; Thong, J. T. L. Low-Contact-Resistance Graphene Devices with Nickel-Etched-Graphene Contacts. *ACS Nano* **2014**, *8*, 994−1001.
(37) Min Song, S.; Yong Kim, T.; Jae Sul, O.; Cheol Shin, W.; Jin Cho, B. Improvement of Graphene−Metal Contact Resistance by Introducing Edge Contacts at Graphene under Metal. *Appl. Phys. Lett.* **2014**, *104*, 183506.
(38) Ito, K.; Ogata, T.; Sakai, T.; Awano, Y. Ultralow Contact Resistivity in Annealed Titanium Edge Contacts for Multilayered Graphene. *Appl. Phys. Express* **2015**, *8*, 025101.
(39) Xia, F.; Mueller, T.; Golizadeh-Mojarad, R.; Freitag, M.; Lin, Y.-m.; Tsang, J.; Perebeinos, V.; Avouris, P. Photocurrent Imaging and Efficient Photon Detection in a Graphene Transistor. *Nano Lett.* **2009**, *9*, 1039−1044.
(40) Ghosh, S.; Sarker, B. K.; Chunder, A.; Zhai, L.; Khondaker, S. I. Position Dependent Photodetector from Large Area Reduced Graphene Oxide Thin Films. *Appl. Phys. Lett.* **2010**, *96*, 163109.
(41) Xia, F.; Mueller, T.; Lin, Y.-m.; Valdes-Garcia, A.; Avouris, P. Ultrafast Graphene Photodetector. *Nat. Nanotechnol.* **2009**, *4*, 839−843.
(42) Urich, A.; Unterrainer, K.; Mueller, T. Intrinsic Response Time of Graphene Photodetectors. *Nano Lett.* **2011**, *11*, 2804−2808.
(43) Prechtel, L.; Song, L.; Schuh, D.; Ajayan, P.; Wegscheider, W.; Holleitner, A. W. Time-Resolved Ultrafast Photocurrents and Terahertz Generation in Freely Suspended Graphene. *Nat. Commun.* **2012**, *3*, 646.
(44) Echtermeyer, T. J.; Nene, P. S.; Trushin, M.; Gorbachev, R. V.; Eiden, A. L.; Milana, S.; Sun, Z.; Schliemann, J.; Lidorikis, E.; Novoselov, K. S.; Ferrari, A. C. Photothermoelectric and Photoelectric Contributions to Light Detection in Metal−Graphene−Metal Photodetectors. *Nano Lett.* **2014**, *14*, 3733−3742.
(45) Tielrooij, K. J.; Massicotte, M.; Piatkowski, L.; Woessner, A.; Ma, Q.; Jarillo-Herrero, P.; Hulst, N. F. v.; Koppens, F. H. L. Hot-Carrier Photocurrent Effects at Graphene−Metal Interfaces. *J. Phys.: Condens. Matter* **2015**, *27*, 164207.
(46) Mueller, T.; Xia, F.; Avouris, P. Graphene Photodetectors for High-Speed Optical Communications. *Nat. Photonics* **2010**, *4*, 297−301.
(47) Cho, B.; Yoon, J.; Lim, S.; Kim, A.; Choi, S.-Y.; Kim, D.-H.; Lee, K.; Lee, B.; Ko, H.; Hahm, M. Metal Decoration Effects on the Gas-Sensing Properties of 2D Hybrid-Structures on Flexible Substrates. *Sensors* **2015**, *15*, 24903−24913.
(48) Cho, B.; Yoon, J.; Hahm, M. G.; Kim, D.-H.; Kim, A. R.; Kahng, Y. H.; Park, S.-W.; Lee, Y.-J.; Park, S.-G.; Kwon, J.-D.; Kim, C. S.; Song, M.; Jeong, Y.; Nam, K.-S.; Ko, H. C. Graphene-Based Gas Sensor: Metal Decoration Effect and Application to a Flexible Device. *J. Mater. Chem. C* **2014**, *2*, 5280−5285.
(49) Vedala, H.; Sorescu, D. C.; Kotchey, G. P.; Star, A. Chemical Sensitivity of Graphene Edges Decorated with Metal Nanoparticles. *Nano Lett.* **2011**, *11*, 2342−2347.
(50) Varghese, S. S.; Lonkar, S.; Singh, K. K.; Swaminathan, S.; Abdala, A. Recent Advances in Graphene Based Gas Sensors. *Sens. Actuators, B* **2015**, *218*, 160−183.
(51) Phan, D.-T.; Chung, G.-S. Effects of Pd Nanocube Size of Pd Nanocube-Graphene Hybrid on Hydrogen Sensing Properties. *Sens. Actuators, B* **2014**, *204*, 437−444.
(52) Alfano, B.; Polichetti, T.; Mauriello, M.; Miglietta, M. L.; Ricciardella, F.; Massera, E.; Di Francia, G. Modulating the Sensing Properties of Graphene through an Eco-Friendly Metal-Decoration Process. *Sens. Actuators, B* **2016**, *222*, 1032−1042.
(53) Chung, M. G.; Kim, D.-H.; Seo, D. K.; Kim, T.; Im, H. U.; Lee, H. M.; Yoo, J.-B.; Hong, S.-H.; Kang, T. J.; Kim, Y. H. Flexible Hydrogen Sensors Using Graphene with Palladium Nanoparticle Decoration. *Sens. Actuators, B* **2012**, *169*, 387−392.
(54) Pak, Y.; Kim, S.-M.; Jeong, H.; Kang, C. G.; Park, J. S.; Song, H.; Lee, R.; Myoung, N.; Lee, B. H.; Seo, S.; Kim, J. T.; Jung, G.-Y. Palladium-Decorated Hydrogen-Gas Sensors Using Periodically Aligned Graphene Nanoribbons. *ACS Appl. Mater. Interfaces* **2014**, *6*, 13293−13298.
(55) Tammanoon, N.; Wisitsoraat, A.; Sriprachuabwong, C.; Phokharatkul, D.; Tuantranont, A.; Phanichphant, S.; Liewhiran, C. Ultrasensitive NO_2 Sensor Based on Ohmic Metal−Semiconductor Interfaces of Electrolytically Exfoliated Graphene/Flame-Spray-Made SnO_2 Nanoparticles Composite Operating at Low Temperatures. *ACS Appl. Mater. Interfaces* **2015**, *7*, 24338−24352.
(56) Chu, B. H.; Nicolosi, J.; Lo, C. F.; Strupinski, W.; Pearton, S. J.; Ren, F. Effect of Coated Platinum Thickness on Hydrogen Detection Sensitivity of Graphene-Based Sensors. *Electrochem. Solid-State Lett.* **2011**, *14*, K43−K45.
(57) Lu, G.; Ocola, E. L.; Chen, J. Reduced Graphene Oxide for Room-Temperature Gas Sensors. *Nanotechnology* **2009**, *20*, 445502.
(58) Liu, H.; Si, M.; Deng, Y.; Neal, A. T.; Du, Y.; Najmaei, S.; Ajayan, P. M.; Lou, J.; Ye, P. D. Switching Mechanism in Single-Layer Molybdenum Disulfide Transistors: An Insight into Current Flow across Schottky Barriers. *ACS Nano* **2014**, *8*, 1031−1038.

DOI: 10.1021/acsnano.6b01842
ACS Nano 2016, 10, 4895−4919

(59) Kang, J.; Liu, W.; Sarkar, D.; Jena, D.; Banerjee, K. Computational Study of Metal Contacts to Monolayer Transition-Metal Dichalcogenide Semiconductors. *Phys. Rev. X* **2014**, *4*, 031005.
(60) Chen, J.-R.; Odenthal, P. M.; Swartz, A. G.; Floyd, G. C.; Wen, H.; Luo, K. Y.; Kawakami, R. K. Control of Schottky Barriers in Single Layer MoS_2 Transistors with Ferromagnetic Contacts. *Nano Lett.* **2013**, *13*, 3106−3110.
(61) Dankert, A.; Langouche, L.; Kamalakar, M. V.; Dash, S. P. High-Performance Molybdenum Disulfide Field-Effect Transistors with Spin Tunnel Contacts. *ACS Nano* **2014**, *8*, 476−482.
(62) Leong, W. S.; Luo, X.; Li, Y.; Khoo, K. H.; Quek, S. Y.; Thong, J. T. L. Low Resistance Metal Contacts to MoS_2 Devices with Nickel-Etched-Graphene Electrodes. *ACS Nano* **2015**, *9*, 869−877.
(63) Gong, C.; Huang, C.; Miller, J.; Cheng, L.; Hao, Y.; Cobden, D.; Kim, J.; Ruoff, R. S.; Wallace, R. M.; Cho, K.; Xu, X.; Chabal, Y. J. Metal Contacts on Physical Vapor Deposited Monolayer MoS_2. *ACS Nano* **2013**, *7*, 11350−11357.
(64) Sun, Y.; Liu, K.; Hong, X.; Chen, M.; Kim, J.; Shi, S.; Wu, J.; Zettl, A.; Wang, F. Probing Local Strain at MX_2−Metal Boundaries with Surface Plasmon-Enhanced Raman Scattering. *Nano Lett.* **2014**, *14*, 5329−5334.
(65) McDonnell, S.; Addou, R.; Buie, C.; Wallace, R. M.; Hinkle, C. L. Defect-Dominated Doping and Contact Resistance in MoS_2. *ACS Nano* **2014**, *8*, 2880−2888.
(66) Chuang, S.; Battaglia, C.; Azcatl, A.; McDonnell, S.; Kang, J. S.; Yin, X.; Tosun, M.; Kapadia, R.; Fang, H.; Wallace, R. M.; Javey, A. MoS_2 *P*-Type Transistors and Diodes Enabled by High Work Function MoO_x Contacts. *Nano Lett.* **2014**, *14*, 1337−1342.
(67) Fang, H.; Chuang, S.; Chang, T. C.; Takei, K.; Takahashi, T.; Javey, A. High-Performance Single Layered WSe_2 *P*-FETs with Chemically Doped Contacts. *Nano Lett.* **2012**, *12*, 3788−3792.
(68) Du, Y.; Yang, L.; Liu, H.; Ye, P. D. Contact Research Strategy for Emerging Molybdenum Disulfide and Other Two-Dimensional Field-Effect Transistors. *APL Mater.* **2014**, *2*, 092510.
(69) Du, Y.; Liu, H.; Deng, Y.; Ye, P. D. Device Perspective for Black Phosphorus Field-Effect Transistors: Contact Resistance, Ambipolar Behavior, and Scaling. *ACS Nano* **2014**, *8*, 10035−10042.
(70) Das, S.; Demarteau, M.; Roelofs, A. Ambipolar Phosphorene Field Effect Transistor. *ACS Nano* **2014**, *8*, 11730−11738.
(71) Haratipour, N.; Robbins, M. C.; Koester, S. J. Black Phosphorus *p*-MOSFETs with 7-nm HfO_2 Gate Dielectric and Low Contact Resistance. *IEEE Electron Device Lett.* **2015**, *36*, 411−413.
(72) Anugrah, Y.; Robbins, M. C.; Crowell, P. A.; Koester, S. J. Determination of the Schottky Barrier Height of Ferromagnetic Contacts to Few-Layer Phosphorene. *Appl. Phys. Lett.* **2015**, *106*, 103108.
(73) Tsai, D.-S.; Liu, K.-K.; Lien, D.-H.; Tsai, M.-L.; Kang, C.-F.; Lin, C.-A.; Li, L.-J.; He, J.-H. Few-Layer MoS_2 with High Broadband Photogain and Fast Optical Switching for Use in Harsh Environments. *ACS Nano* **2013**, *7*, 3905−3911.
(74) Tsai, D. S.; Lien, D. H.; Tsai, M. L.; Su, S. H.; Chen, K. M.; Ke, J. J.; Yu, Y. C.; Li, L. J.; He, J. H. Trilayered MoS_2 Metal Semiconductor Metal Photodetectors: Photogain and Radiation Resistance. *IEEE J. Sel. Top. Quantum Electron.* **2014**, *20*, 30−35.
(75) Cai, X.; Sushkov, A. B.; Suess, R. J.; Jadidi, M. M.; Jenkins, G. S.; Nyakiti, L. O.; Myers-Ward, R. L.; Li, S.; Yan, J.; Gaskill, D. K.; Murphy, T. E.; Drew, H. D.; Fuhrer, M. S. Sensitive Room-Temperature Terahertz Detection *Via* the Photothermoelectric Effect in Graphene. *Nat. Nanotechnol.* **2014**, *9*, 814−819.
(76) Zhang, Y.; Li, H.; Wang, L.; Wang, H.; Xie, X.; Zhang, S.-L.; Liu, R.; Qiu, Z.-J. Photothermoelectric and Photovoltaic Effects Both Present in MoS_2. *Sci. Rep.* **2015**, *5*, 7938.
(77) Cao, Y.; Cai, K.; Hu, P.; Zhao, L.; Yan, T.; Luo, W.; Zhang, X.; Wu, X.; Wang, K.; Zheng, H. Strong Enhancement of Photoresponsivity with Shrinking the Electrodes Spacing in Few Layer Gase Photodetectors. *Sci. Rep.* **2015**, *5*, 8130.
(78) Zhang, W.; Chiu, M.-H.; Chen, C.-H.; Chen, W.; Li, L.-J.; Wee, A. T. S. Role of Metal Contacts in High-Performance Phototransistors Based on WSe_2 Monolayers. *ACS Nano* **2014**, *8*, 8653−8661.
(79) Zhang, W.; Huang, J.-K.; Chen, C.-H.; Chang, Y.-H.; Cheng, Y.-J.; Li, L.-J. High-Gain Phototransistors Based on a CVD MoS_2 Monolayer. *Adv. Mater.* **2013**, *25*, 3456−3461.
(80) Liu, W.; Kang, J.; Sarkar, D.; Khatami, Y.; Jena, D.; Banerjee, K. Role of Metal Contacts in Designing High-Performance Monolayer *N*-Type WSe_2 Field Effect Transistors. *Nano Lett.* **2013**, *13*, 1983−1990.
(81) Britnell, L.; Ribeiro, R. M.; Eckmann, A.; Jalil, R.; Belle, B. D.; Mishchenko, A.; Kim, Y. J.; Gorbachev, R. V.; Georgiou, T.; Morozov, S. V.; Grigorenko, A. N.; Geim, A. K.; Casiraghi, C.; Neto, A. H. C.; Novoselov, K. S. Strong Light-Matter Interactions in Heterostructures of Atomically Thin Films. *Science* **2013**, *340*, 1311−1314.
(82) Eda, G.; Maier, S. A. Two-Dimensional Crystals: Managing Light for Optoelectronics. *ACS Nano* **2013**, *7*, 5660−5665.
(83) Kern, J.; Trügler, A.; Niehues, I.; Ewering, J.; Schmidt, R.; Schneider, R.; Najmaei, S.; George, A.; Zhang, J.; Lou, J.; Hohenester, U.; Michaelis de Vasconcellos, S.; Bratschitsch, R. Nanoantenna-Enhanced Light−Matter Interaction in Atomically Thin WS_2. *ACS Photonics* **2015**, *2*, 1260−1265.
(84) Butun, S.; Tongay, S.; Aydin, K. Enhanced Light Emission from Large-Area Monolayer MoS_2 Using Plasmonic Nanodisc Arrays. *Nano Lett.* **2015**, *15*, 2700−2704.
(85) Kannan, P. K.; Late, D. J.; Morgan, H.; Rout, C. S. Recent Developments in 2D Layered Inorganic Nanomaterials for Sensing. *Nanoscale* **2015**, *7*, 13293−13312.
(86) Late, D. J.; Doneux, T.; Bougouma, M. Single-Layer $MoSe_2$ Based NH_3 Gas Sensor. *Appl. Phys. Lett.* **2014**, *105*, 233103.
(87) Mayorga-Martinez, C. C.; Ambrosi, A.; Eng, A. Y. S.; Sofer, Z.; Pumera, M. Metallic 1T-WS_2 for Selective Impedimetric Vapor Sensing. *Adv. Funct. Mater.* **2015**, *25*, 5611−5616.
(88) Ou, J. Z.; Ge, W.; Carey, B.; Daeneke, T.; Rotbart, A.; Shan, W.; Wang, Y.; Fu, Z.; Chrimes, A. F.; Wlodarski, W.; Russo, S. P.; Li, Y. X.; Kalantar-zadeh, K. Physisorption-Based Charge Transfer in Two-Dimensional SnS_2 for Selective and Reversible NO_2 Gas Sensing. *ACS Nano* **2015**, *9*, 10313−10323.
(89) Franke, M. E.; Koplin, T. J.; Simon, U. Metal and Metal Oxide Nanoparticles in Chemiresistors: Does the Nanoscale Matter? *Small* **2006**, *2*, 36−50.
(90) Fang, H.; Tosun, M.; Seol, G.; Chang, T. C.; Takei, K.; Guo, J.; Javey, A. Degenerate *N*-Doping of Few-Layer Transition Metal Dichalcogenides by Potassium. *Nano Lett.* **2013**, *13*, 1991−1995.
(91) Liu, B.; Chen, L.; Liu, G.; Abbas, A. N.; Fathi, M.; Zhou, C. High-Performance Chemical Sensing Using Schottky-Contacted Chemical Vapor Deposition Grown Monolayer MoS_2 Transistors. *ACS Nano* **2014**, *8*, 5304−5314.
(92) Abbas, A. N.; Liu, B.; Chen, L.; Ma, Y.; Cong, S.; Aroonyadet, N.; Köpf, M.; Nilges, T.; Zhou, C. Black Phosphorus Gas Sensors. *ACS Nano* **2015**, *9*, 5618−5624.
(93) Alsaif, M. M. Y. A.; Balendhran, S.; Field, M. R.; Latham, K.; Wlodarski, W.; Ou, J. Z.; Kalantar-zadeh, K. Two Dimensional α-MoO_3 Nanoflakes Obtained Using Solvent-Assisted Grinding and Sonication Method: Application for H_2 Gas Sensing. *Sens. Actuators, B* **2014**, *192*, 196−204.
(94) Shanmugam, M.; Durcan, C. A.; Yu, B. Layered Semiconductor Molybdenum Disulfide Nanomembrane Based Schottky-Barrier Solar Cells. *Nanoscale* **2012**, *4*, 7399−7405.
(95) Wi, S.; Kim, H.; Chen, M.; Nam, H.; Guo, L. J.; Meyhofer, E.; Liang, X. Enhancement of Photovoltaic Response in Multilayer MoS_2 Induced by Plasma Doping. *ACS Nano* **2014**, *8*, 5270−5281.
(96) Buscema, M.; Groenendijk, D. J.; Steele, G. A.; van der Zant, H. S. J.; Castellanos-Gomez, A. Photovoltaic Effect in Few-Layer Black Phosphorus *PN* Junctions Defined by Local Electrostatic Gating. *Nat. Commun.* **2014**, *5*, 4651.
(97) Baugher, B. W. H.; Churchill, H. O. H.; Yang, Y.; Jarillo-Herrero, P. Optoelectronic Devices Based on Electrically Tunable *P-N* Diodes in a Monolayer Dichalcogenide. *Nat. Nanotechnol.* **2014**, *9*, 262−267.
(98) Tongay, S.; Schumann, T.; Hebard, A. F. Graphite Based Schottky Diodes Formed on Si, GaAs, and 4H-SiC Substrates. *Appl. Phys. Lett.* **2009**, *95*, 222103.

DOI: 10.1021/acsnano.6b01842
ACS Nano 2016, 10, 4895−4919

(99) Parui, S.; Ruiter, R.; Zomer, P. J.; Wojtaszek, M.; van Wees, B. J.; Banerjee, T. Temperature Dependent Transport Characteristics of Graphene/*N*-Si Diodes. *J. Appl. Phys.* **2014**, *116*, 244505.
(100) Yim, C.; McEvoy, N.; Duesberg, G. S. Characterization of Graphene-Silicon Schottky Barrier Diodes Using Impedance Spectroscopy. *Appl. Phys. Lett.* **2013**, *103*, 193106.
(101) Fattah, A.; Khatami, S.; Mayorga-Martinez, C. C.; Medina-Sánchez, M.; Baptista-Pires, L.; Merkoçi, A. Graphene/Silicon Heterojunction Schottky Diode for Vapors Sensing Using Impedance Spectroscopy. *Small* **2014**, *10*, 4193−4199.
(102) Chen, C.-C.; Aykol, M.; Chang, C.-C.; Levi, A. F. J.; Cronin, S. B. Graphene-Silicon Schottky Diodes. *Nano Lett.* **2011**, *11*, 1863−1867.
(103) Tongay, S.; Lemaitre, M.; Schumann, T.; Berke, K.; Appleton, B. R.; Gila, B.; Hebard, A. F. Graphene/GaN Schottky Diodes: Stability at Elevated Temperatures. *Appl. Phys. Lett.* **2011**, *99*, 102102.
(104) Fisichella, G.; Greco, G.; Roccaforte, F.; Giannazzo, F. Current Transport in Graphene/AlGaN/GaN Vertical Heterostructures Probed at Nanoscale. *Nanoscale* **2014**, *6*, 8671−8680.
(105) Tadjer, M. J.; Anderson, T. J.; Hobart, K. D.; Nyakiti, L. O.; Wheeler, V. D.; Myers-Ward, R. L.; Gaskill, D. K.; Eddy, C. R.; Kub, F. J.; Calle, F. Vertical Conduction Mechanism of the Epitaxial Graphene/*N*-Type 4H-SiC Heterojunction at Cryogenic Temperatures. *Appl. Phys. Lett.* **2012**, *100*, 193506.
(106) Dharmaraj, P.; Jeganathan, K.; Parthiban, S.; Kwon, J. Y.; Gautam, S.; Chae, K. H.; Asokan, K. Selective Area Growth of Bernal Bilayer Epitaxial Graphene on 4H-SiC (0001) Substrate by Electron-Beam Irradiation. *Appl. Phys. Lett.* **2014**, *105*, 181601.
(107) Tomer, D.; Rajput, S.; Hudy, L. J.; Li, C. H.; Li, L. Intrinsic Inhomogeneity in Barrier Height at Monolayer Graphene/SiC Schottky Junction. *Appl. Phys. Lett.* **2014**, *105*, 021607.
(108) Sonde, S.; Giannazzo, F.; Raineri, V.; Yakimova, R.; Huntzinger, J. R.; Tiberj, A.; Camassel, J. Electrical Properties of the Graphene/4H-SiC (0001) Interface Probed by Scanning Current Spectroscopy. *Phys. Rev. B: Condens. Matter Mater. Phys.* **2009**, *80*, 241406.
(109) Lee, S.; Lee, Y.; Young Kim, D.; Song, E. B.; Min Kim, S. Back-Gate Tuning of Schottky Barrier Height in Graphene/Zinc-Oxide Photodiodes. *Appl. Phys. Lett.* **2013**, *102*, 242114.
(110) Tongay, S.; Lemaitre, M.; Miao, X.; Gila, B.; Appleton, B. R.; Hebard, A. F. Rectification at Graphene-Semiconductor Interfaces: Zero-Gap Semiconductor-Based Diodes. *Phys. Rev. X* **2012**, *2*, 011002.
(111) Yang, H.; Heo, J.; Park, S.; Song, H. J.; Seo, D. H.; Byun, K.-E.; Kim, P.; Yoo, I.; Chung, H.-J.; Kim, K. Graphene Barristor, a Triode Device with a Gate-Controlled Schottky Barrier. *Science* **2012**, *336*, 1140−1143.
(112) Chen, C.-C.; Chang, C.-C.; Li, Z.; Levi, A. F. J.; Cronin, S. B. Gate Tunable Graphene-Silicon Ohmic/Schottky Contacts. *Appl. Phys. Lett.* **2012**, *101*, 223113.
(113) Cavallo, F.; Rojas Delgado, R.; Kelly, M. M.; Sánchez Pérez, J. R.; Schroeder, D. P.; Xing, H. G.; Eriksson, M. A.; Lagally, M. G. Exceptional Charge Transport Properties of Graphene on Germanium. *ACS Nano* **2014**, *8*, 10237−10245.
(114) Baek, S.-h. C.; Seo, Y.-J.; Oh, J. G.; Albert Park, M. G.; Bong, J. H.; Yoon, S. J.; Seo, M.; Park, S.-y.; Park, B.-G.; Lee, S.-H. Alleviation of Fermi-Level Pinning Effect at Metal/Germanium Interface by the Insertion of Graphene Layers. *Appl. Phys. Lett.* **2014**, *105*, 073508.
(115) Shiu, H. W.; Chang, L. Y.; Lee, K.-H.; Chen, H.-Y.; Gwo, S.; Chen, C.-H. Graphene as Tunable Transparent Electrode Material on GaN: Layer-Number-Dependent Optical and Electrical Properties. *Appl. Phys. Lett.* **2013**, *103*, 081604.
(116) Liu, X.; Luo, X.; Nan, H.; Guo, H.; Wang, P.; Zhang, L.; Zhou, M.; Yang, Z.; Shi, Y.; Hu, W.; Ni, Z.; Qiu, T.; Yu, Z.; Xu, J.; Wang, X. Epitaxial Ultrathin Organic Crystals on Graphene for High-Efficiency Phototransistors. *Adv. Mater.* **2016**, in press.
(117) Zhang, Y.; Qiao, J.; Gao, S.; Hu, F.; He, D.; Wu, B.; Yang, Z.; Xu, B.; Li, Y.; Shi, Y.; Ji, W.; Wang, P.; Wang, X.; Xiao, M.; Xu, H.; Xu, J.-B.; Wang, X. Probing Carrier Transport and Structure-Property Relationship of Highly Ordered Organic Semiconductors at the Two-Dimensional Limit. *Phys. Rev. Lett.* **2016**, *116*, 016602.
(118) He, D.; Zhang, Y.; Wu, Q.; Xu, R.; Nan, H.; Liu, J.; Yao, J.; Wang, Z.; Yuan, S.; Li, Y.; Shi, Y.; Wang, J.; Ni, Z.; He, L.; Miao, F.; Song, F.; Xu, H.; Watanabe, K.; Taniguchi, T.; Xu, J.-B.; et al. Two-Dimensional Quasi-Freestanding Molecular Crystals for High-Performance Organic Field-Effect Transistors. *Nat. Commun.* **2014**, *5*, 5162.
(119) Giannazzo, F.; Roccaforte, F.; Iucolano, F.; Raineri, V.; Ruffino, F.; Grimaldi, M. G. Nanoscale Current Transport through Schottky Contacts on Wide Bandgap Semiconductors. *J. Vac. Sci. Technol. B* **2009**, *27*, 789−794.
(120) Fisichella, G.; Greco, G.; Roccaforte, F.; Giannazzo, F. From Schottky to Ohmic Graphene Contacts to AlGaN/GaN Heterostructures: Role of the AlGaN Layer Microstructure. *Appl. Phys. Lett.* **2014**, *105*, 063117.
(121) Zhong, H.; Xu, K.; Liu, Z.; Xu, G.; Shi, L.; Fan, Y.; Wang, J.; Ren, G.; Yang, H. Charge Transport Mechanisms of Graphene/Semiconductor Schottky Barriers: A Theoretical and Experimental Study. *J. Appl. Phys.* **2014**, *115*, 013701.
(122) Shivaraman, S.; Herman, L. H.; Rana, F.; Park, J.; Spencer, M. G. Schottky Barrier Inhomogeneities at the Interface of Few Layer Epitaxial Graphene and Silicon Carbide. *Appl. Phys. Lett.* **2012**, *100*, 183112.
(123) Werner, J. H.; Güttler, H. H. Barrier Inhomogeneities at Schottky Contacts. *J. Appl. Phys.* **1991**, *69*, 1522−1533.
(124) Tung, R. T. Electron Transport at Metal-Semiconductor Interfaces: General Theory. *Phys. Rev. B: Condens. Matter Mater. Phys.* **1992**, *45*, 13509−13523.
(125) An, Y.; Behnam, A.; Pop, E.; Ural, A. Metal-Semiconductor-Metal Photodetectors Based on Graphene/*P*-Type Silicon Schottky Junctions. *Appl. Phys. Lett.* **2013**, *102*, 013110.
(126) Sinha, D.; Lee, J. U. Ideal Graphene/Silicon Schottky Junction Diodes. *Nano Lett.* **2014**, *14*, 4660−4664.
(127) Zeng, L.-H.; Wang, M.-Z.; Hu, H.; Nie, B.; Yu, Y.-Q.; Wu, C.-Y.; Wang, L.; Hu, J.-G.; Xie, C.; Liang, F.-X.; Luo, L.-B. Monolayer Graphene/Germanium Schottky Junction as High-Performance Self-Driven Infrared Light Photodetector. *ACS Appl. Mater. Interfaces* **2013**, *5*, 9362−9366.
(128) Amirmazlaghani, M.; Raissi, F.; Habibpour, O.; Vukusic, J.; Stake, J. Graphene-Si Schottky IR Detector. *IEEE J. Quantum Electron.* **2013**, *49*, 589−594.
(129) Lv, P.; Zhang, X.; Zhang, X.; Deng, W.; Jie, J. High-Sensitivity and Fast-Response Graphene/Crystalline Silicon Schottky Junction-Based Near-IR Photodetectors. *IEEE Electron Device Lett.* **2013**, *34*, 1337−1339.
(130) An, X.; Liu, F.; Jung, Y. J.; Kar, S. Tunable Graphene−Silicon Heterojunctions for Ultrasensitive Photodetection. *Nano Lett.* **2013**, *13*, 909−916.
(131) Luo, L.-B.; Chen, J.-J.; Wang, M.-Z.; Hu, H.; Wu, C.-Y.; Li, Q.; Wang, L.; Huang, J.-A.; Liang, F.-X. Near-Infrared Light Photovoltaic Detector Based on GaAs Nanocone Array/Monolayer Graphene Schottky Junction. *Adv. Funct. Mater.* **2014**, *24*, 2794−2800.
(132) Liu, H.; Sun, Q.; Xing, J.; Zheng, Z.; Zhang, Z.; Lü, Z.; Zhao, K. Fast and Enhanced Broadband Photoresponse of a ZnO Nanowire Array/Reduced Graphene Oxide Film Hybrid Photodetector from the Visible to the Near-Infrared Range. *ACS Appl. Mater. Interfaces* **2015**, *7*, 6645−6651.
(133) Zhang, Z.; Guo, Y.; Wang, X.; Li, D.; Wang, F.; Xie, S. Direct Growth of Nanocrystalline Graphene/Graphite Transparent Electrodes on Si/SiO_2 for Metal-Free Schottky Junction Photodetectors. *Adv. Funct. Mater.* **2014**, *24*, 835−840.
(134) Zhu, M.; Li, X.; Guo, Y.; Li, X.; Sun, P.; Zang, X.; Wang, K.; Zhong, M.; Wu, D.; Zhu, H. Vertical Junction Photodetectors Based on Reduced Graphene Oxide/Silicon Schottky Diodes. *Nanoscale* **2014**, *6*, 4909−4914.
(135) Kim, J.; Joo, S. S.; Lee, K. W.; Kim, J. H.; Shin, D. H.; Kim, S.; Choi, S.-H. Near-Ultraviolet-Sensitive Graphene/Porous Silicon Photodetectors. *ACS Appl. Mater. Interfaces* **2014**, *6*, 20880−20886.

DOI: 10.1021/acsnano.6b01842
ACS Nano 2016, 10, 4895−4919

(136) Nie, B.; Hu, J.-G.; Luo, L.-B.; Xie, C.; Zeng, L.-H.; Lv, P.; Li, F.-Z.; Jie, J.-S.; Feng, M.; Wu, C.-Y.; Yu, Y.-Q.; Yu, S.-H. Monolayer Graphene Film on ZnO Nanorod Array for High-Performance Schottky Junction Ultraviolet Photodetectors. *Small* **2013**, *9*, 2872−2879.
(137) Liu, X.; Ji, X.; Liu, M.; Liu, N.; Tao, Z.; Dai, Q.; Wei, L.; Li, C.; Zhang, X.; Wang, B. High-Performance Ge Quantum Dot Decorated Graphene/Zinc-Oxide Heterostructure Infrared Photodetector. *ACS Appl. Mater. Interfaces* **2015**, *7*, 2452−2458.
(138) Kim, H.-Y.; Lee, K.; McEvoy, N.; Yim, C.; Duesberg, G. S. Chemically Modulated Graphene Diodes. *Nano Lett.* **2013**, *13*, 2182−2188.
(139) Uddin, M. A.; Singh, A. K.; Sudarshan, S. T.; Koley, G. Functionalized Graphene/Silicon Chemi-Diode H_2 Sensor with Tunable Sensitivity. *Nanotechnology* **2014**, *25*, 125501.
(140) Singh, A.; Uddin, M. A.; Sudarshan, T.; Koley, G. Tunable Reverse-Biased Graphene/Silicon Heterojunction Schottky Diode Sensor. *Small* **2014**, *10*, 1555−1565.
(141) Kim, J.; Oh, S. D.; Kim, J. H.; Shin, D. H.; Kim, S.; Choi, S.-H. Graphene/Si-Nanowire Heterostructure Molecular Sensors. *Sci. Rep.* **2014**, *4*, 5384.
(142) Zhu, M.; Li, X.; Chung, S.; Zhao, L.; Li, X.; Zang, X.; Wang, K.; Wei, J.; Zhong, M.; Zhou, K.; Xie, D.; Zhu, H. Photo-Induced Selective Gas Detection Based on Reduced Graphene Oxide/Si Schottky Diode. *Carbon* **2015**, *84*, 138−145.
(143) Li, X.; Zhu, H.; Wang, K.; Cao, A.; Wei, J.; Li, C.; Jia, Y.; Li, Z.; Li, X.; Wu, D. Graphene-on-Silicon Schottky Junction Solar Cells. *Adv. Mater.* **2010**, *22*, 2743−2748.
(144) Fan, G.; Zhu, H.; Wang, K.; Wei, J.; Li, X.; Shu, Q.; Guo, N.; Wu, D. Graphene/Silicon Nanowire Schottky Junction for Enhanced Light Harvesting. *ACS Appl. Mater. Interfaces* **2011**, *3*, 721−725.
(145) Xie, C.; Lv, P.; Nie, B.; Jie, J.; Zhang, X.; Wang, Z.; Jiang, P.; Hu, Z.; Luo, L.; Zhu, Z.; Wang, L.; Wu, C. Monolayer Graphene Film/Silicon Nanowire Array Schottky Junction Solar Cells. *Appl. Phys. Lett.* **2011**, *99*, 133113.
(146) Feng, T.; Xie, D.; Lin, Y.; Zhao, H.; Chen, Y.; Tian, H.; Ren, T.; Li, X.; Li, Z.; Wang, K.; Wu, D.; Zhu, H. Efficiency Enhancement of Graphene/Silicon-Pillar-Array Solar Cells by HNO_3 and PEDOT-PSS. *Nanoscale* **2012**, *4*, 2130−2133.
(147) Miao, X.; Tongay, S.; Petterson, M. K.; Berke, K.; Rinzler, A. G.; Appleton, B. R.; Hebard, A. F. High Efficiency Graphene Solar Cells by Chemical Doping. *Nano Lett.* **2012**, *12*, 2745−2750.
(148) Cui, T.; Lv, R.; Huang, Z.-H.; Chen, S.; Zhang, Z.; Gan, X.; Jia, Y.; Li, X.; Wang, K.; Wu, D.; Kang, F. Enhanced Efficiency of Graphene/Silicon Heterojunction Solar Cells by Molecular Doping. *J. Mater. Chem. A* **2013**, *1*, 5736−5740.
(149) Xie, C.; Zhang, X.; Wu, Y.; Zhang, X.; Zhang, X.; Wang, Y.; Zhang, W.; Gao, P.; Han, Y.; Jie, J. Surface Passivation and Band Engineering: A Way toward High Efficiency Graphene-Planar Si Solar Cells. *J. Mater. Chem. A* **2013**, *1*, 8567−8574.
(150) Li, X.; Xie, D.; Park, H.; Zhu, M.; Zeng, T. H.; Wang, K.; Wei, J.; Wu, D.; Kong, J.; Zhu, H. Ion Doping of Graphene for High-Efficiency Heterojunction Solar Cells. *Nanoscale* **2013**, *5*, 1945−1948.
(151) Ho, P.-H.; Liou, Y.-T.; Chuang, C.-H.; Lin, S.-W.; Tseng, C.-Y.; Wang, D.-Y.; Chen, C.-C.; Hung, W.-Y.; Wen, C.-Y.; Chen, C.-W. Self-Crack-Filled Graphene Films by Metallic Nanoparticles for High-Performance Graphene Heterojunction Solar Cells. *Adv. Mater.* **2015**, *27*, 1724−1729.
(152) Song, Y.; Li, X.; Mackin, C.; Zhang, X.; Fang, W.; Palacios, T.; Zhu, H.; Kong, J. Role of Interfacial Oxide in High-Efficiency Graphene−Silicon Schottky Barrier Solar Cells. *Nano Lett.* **2015**, *15*, 2104−2110.
(153) Vazquez-Mena, O.; Bosco, J. P.; Ergen, O.; Rasool, H. I.; Fathalizadeh, A.; Tosun, M.; Crommie, M.; Javey, A.; Atwater, H. A.; Zettl, A. Performance Enhancement of a Graphene-Zinc Phosphide Solar Cell Using the Electric Field-Effect. *Nano Lett.* **2014**, *14*, 4280−4285.
(154) Yan, K.; Wei, Z.; Li, J.; Chen, H.; Yi, Y.; Zheng, X.; Long, X.; Wang, Z.; Wang, J.; Xu, J.; Yang, S. High-Performance Graphene-Based Hole Conductor-Free Perovskite Solar Cells: Schottky Junction Enhanced Hole Extraction and Electron Blocking. *Small* **2015**, *11*, 2269−2274.
(155) Lee, E. W.; Ma, L.; Nath, D. N.; Lee, C. H.; Arehart, A.; Wu, Y.; Rajan, S. Growth and Electrical Characterization of Two-Dimensional Layered MoS_2/SiC Heterojunctions. *Appl. Phys. Lett.* **2014**, *105*, 203504.
(156) Chuang, S.; Kapadia, R.; Fang, H.; Chia Chang, T.; Yen, W.-C.; Chueh, Y.-L.; Javey, A. Near-Ideal Electrical Properties of InAs/WSe_2 Van Der Waals Heterojunction Diodes. *Appl. Phys. Lett.* **2013**, *102*, 242101.
(157) Yim, C.; O'Brien, M.; McEvoy, N.; Riazimehr, S.; Schäfer-Eberwein, H.; Bablich, A.; Pawar, R.; Iannaccone, G.; Downing, C.; Fiori, G.; Lemme, M. C.; Duesberg, G. S. Heterojunction Hybrid Devices from Vapor Phase Grown MoS_2. *Sci. Rep.* **2014**, *4*, 5458.
(158) Esmaeili-Rad, M. R.; Salahuddin, S. High Performance Molybdenum Disulfide Amorphous Silicon Heterojunction Photodetector. *Sci. Rep.* **2013**, *3*, 2345.
(159) Li, Y.; Xu, C.-Y.; Wang, J.-Y.; Zhen, L. Photodiode-Like Behavior and Excellent Photoresponse of Vertical Si/Monolayer MoS_2 Heterostructures. *Sci. Rep.* **2014**, *4*, 7186.
(160) Wang, L.; Jie, J.; Shao, Z.; Zhang, Q.; Zhang, X.; Wang, Y.; Sun, Z.; Lee, S.-T. MoS_2/Si Heterojunction with Vertically Standing Layered Structure for Ultrafast, High-Detectivity, Self-Driven Visible−Near Infrared Photodetectors. *Adv. Funct. Mater.* **2015**, *25*, 2910−2919.
(161) Lopez-Sanchez, O.; Alarcon Llado, E.; Koman, V.; Fontcuberta i Morral, A.; Radenovic, A.; Kis, A. Light Generation and Harvesting in a Van Der Waals Heterostructure. *ACS Nano* **2014**, *8*, 3042−3048.
(162) Tsai, M.-L.; Su, S.-H.; Chang, J.-K.; Tsai, D.-S.; Chen, C.-H.; Wu, C.-I.; Li, L.-J.; Chen, L.-J.; He, J.-H. Monolayer MoS_2 Heterojunction Solar Cells. *ACS Nano* **2014**, *8*, 8317−8322.
(163) Hao, L.; Liu, Y.; Gao, W.; Han, Z.; Xue, Q.; Zeng, H.; Wu, Z.; Zhu, J.; Zhang, W. Electrical and Photovoltaic Characteristics of MoS_2/Si *P-N* Junctions. *J. Appl. Phys.* **2015**, *117*, 114502.
(164) Tao, L.; Cinquanta, E.; Chiappe, D.; Grazianetti, C.; Fanciulli, M.; Dubey, M.; Molle, A.; Akinwande, D. Silicene Field-Effect Transistors Operating at Room Temperature. *Nat. Nanotechnol.* **2015**, *10*, 227−231.
(165) Derivaz, M.; Dentel, D.; Stephan, R.; Hanf, M.-C.; Mehdaoui, A.; Sonnet, P.; Pirri, C. Continuous Germanene Layer on Al(111). *Nano Lett.* **2015**, *15*, 2510−2516.
(166) Lin, Z.; He, Q.; Yin, A.; Xu, Y.; Wang, C.; Ding, M.; Cheng, H.-C.; Papandrea, B.; Huang, Y.; Duan, X. Cosolvent Approach for Solution-Processable Electronic Thin Films. *ACS Nano* **2015**, *9*, 4398−4405.
(167) Torrisi, F.; Hasan, T.; Wu, W.; Sun, Z.; Lombardo, A.; Kulmala, T. S.; Hsieh, G.-W.; Jung, S.; Bonaccorso, F.; Paul, P. J.; Chu, D.; Ferrari, A. C. Inkjet-Printed Graphene Electronics. *ACS Nano* **2012**, *6*, 2992−3006.
(168) Secor, E. B.; Lim, S.; Zhang, H.; Frisbie, C. D.; Francis, L. F.; Hersam, M. C. Gravure Printing of Graphene for Large-Area Flexible Electronics. *Adv. Mater.* **2014**, *26*, 4533−4538.
(169) Hurch, S.; Nolan, H.; Hallam, T.; Berner, N. C.; McEvoy, N.; Duesberg, G. S. Inkjet-Defined Field-Effect Transistors from Chemical Vapour Deposited Graphene. *Carbon* **2014**, *71*, 332−337.
(170) Withers, F.; Yang, H.; Britnell, L.; Rooney, A. P.; Lewis, E.; Felten, A.; Woods, C. R.; Sanchez Romaguera, V.; Georgiou, T.; Eckmann, A.; Kim, Y. J.; Yeates, S. G.; Haigh, S. J.; Geim, A. K.; Novoselov, K. S.; Casiraghi, C. Heterostructures Produced from Nanosheet-Based Inks. *Nano Lett.* **2014**, *14*, 3987−3992.
(171) Torrisi, F.; Coleman, J. N. Electrifying Inks with 2D Materials. *Nat. Nanotechnol.* **2014**, *9*, 738−739.
(172) Liu, Y.; Wu, H.; Cheng, H.-C.; Yang, S.; Zhu, E.; He, Q.; Ding, M.; Li, D.; Guo, J.; Weiss, N. O.; Huang, Y.; Duan, X. Toward Barrier Free Contact to Molybdenum Disulfide Using Graphene Electrodes. *Nano Lett.* **2015**, *15*, 3030−3034.

DOI: 10.1021/acsnano.6b01842
ACS Nano 2016, 10, 4895−4919

(173) Voiry, D.; Mohite, A.; Chhowalla, M. Phase Engineering of Transition Metal Dichalcogenides. *Chem. Soc. Rev.* **2015**, *44*, 2702−2712.
(174) Cho, S.; Kim, S.; Kim, J. H.; Zhao, J.; Seok, J.; Keum, D. H.; Baik, J.; Choe, D.-H.; Chang, K. J.; Suenaga, K.; Kim, S. W.; Lee, Y. H.; Yang, H. Phase Patterning for Ohmic Homojunction Contact in $MoTe_2$. *Science* **2015**, *349*, 625−628.
(175) Kappera, R.; Voiry, D.; Yalcin, S. E.; Branch, B.; Gupta, G.; Mohite, A. D.; Chhowalla, M. Phase-Engineered Low-Resistance Contacts for Ultrathin MoS_2 Transistors. *Nat. Mater.* **2014**, *13*, 1128−1134.
(176) Ma, Y.; Liu, B.; Zhang, A.; Chen, L.; Fathi, M.; Shen, C.; Abbas, A. N.; Ge, M.; Mecklenburg, M.; Zhou, C. Reversible Semiconducting-to-Metallic Phase Transition in Chemical Vapor Deposition Grown Monolayer WSe_2 and Applications for Devices. *ACS Nano* **2015**, *9*, 7383−7391.

DOI: 10.1021/acsnano.6b01842
ACS Nano 2016, 10, 4895−4919